A&A, 711, A287 (2026)
https://doi.org/10.1051/0004-6361/202659670

Astronomy & Astrophysics

Untangling dust emission and cosmic infrared background anisotropies with the scattering transform statistics

Srijita Sinha[1,2,⋆], Tuhin Ghosh[1,2,⋆], Erwan Allys[3], François Boulanger[3], and Jean-Marc Delouis[4]

[1] School for Physical Sciences, National Institute of Science Education and Research, HBNI Jatni-752050, India
[2] Homi Bhabha National Institute, Training School Complex, Anushakti Nagar, Mumbai 400094, India
[3] Laboratoire de Physique de l'École Normale Supérieure, ENS, Université PSL, CNRS, Sorbonne Université, Université Paris Cité, 75005 Paris, France
[4] Laboratoire d'Océanographie Physique et Spatiale (LOPS), Univ. Brest, CNRS, Ifremer, IRD, 29200 Brest, France

Received 2 March 2026 / Accepted 27 May 2026

ABSTRACT

Context. A template-fit approach is often used to separate the Galactic dust emission and the cosmic infrared background (CIB) anisotropies in low H I column density regions using the observational fact that the 21 cm H I line emission from neutral atomic hydrogen and dust are tightly correlated. However, in some regions with molecular hydrogen, diffuse ionised gas, and dark gas, the same approach fails to trace the excess Galactic dust emission.

Aims. We developed and tested a statistical component-separation method to extract the dust signal from the contaminated *Planck* 353 GHz observations using the scattering covariance (SC) statistics, which is a subclass of scattering transform statistics.

Methods. We first obtained a set CIB maps over 25 square patches, each with a sky area of 222 deg^2, using the linear correlation of dust and Galactic H I column density map valid in low H I column density regions using the template-fit approach. We then constructed from these 25 maps a generative model of CIB using SC statistics. We finally relied on this generative model to perform a component-separation of dust and CIB in the *Planck* data for different sky regions. These separations were achieved by sampling an ensemble of dust maps through pixel-based optimisation, which, when added to the CIB contamination model, verified all the statistics and cross statistics constraints that were estimated directly from the data.

Results. We validated our algorithm and separated the dust emission from the contamination in the *Planck* 353 GHz observations. We show the results of the recovered dust map for a test sky region where there is a significant difference between the *Planck* dust map and CSFD map. We found that the *Planck* dust map has more structure than the CSFD map. We compared the power spectrum of the recovered dust map and H I map and found a difference in slope ($\Delta\alpha \approx 0.4$) by fitting a power-law model to the two spectra. To explain $\Delta\alpha$, we decomposed the recovered dust map into two gas phases: dust associated with neutral atomic hydrogen, and dust associated with molecular hydrogen. We provide a clear pathway to mapping the Galactic interstellar reddening over intermediate and high Galactic latitudes.

Key words. methods: statistical – dust, extinction – infrared: diffuse background – submillimeter: diffuse background

1. Introduction

The cosmic microwave background (CMB) signal encoding the history of the Universe at microwave and far-infrared frequencies is buried deep below the large-scale emission from the Galaxy and the small-scale emission from the extra-galactic sources (Ichiki 2014). At frequencies above 200 GHz, diffuse thermal emission from our own Galaxy and cosmic infrared background (CIB; Puget et al. 1996; Lagache et al. 2005) are the primary contributors to foreground emission (Planck 2018 results. IV. 2020). Galactic thermal dust emission provides a wealth of information regarding the complex physical systems that form the interstellar medium (ISM) (Draine 2011). The CIB is the diffuse radiation from dust particles in star-forming galaxies through the evolution of the Universe, and it acts as a probe for the dark matter distribution and star formation history (Hauser & Dwek 2001; Planck 2013 results. XXX. 2014; Maniyar, A. S. et al. 2018). Moreover, the CIB plays a vital role in de-lensing the observed CMB B modes (Larsen et al. 2016).

Although they have very different origins, dust emission and the CIB share a similar spectral energy distribution; both follow a modified blackbody spectrum with a slightly different spectral index. Separating these two components is challenging using spectral information alone.

Galactic thermal dust emission was observed to be tightly correlated with the 21 cm H I emission in low H I column density regions (Boulanger et al. 1996; Boulanger & Perault 1988). For this reason, the H I emission map is often used as a tracer of the dust emission within a template-fit approach to separate it from the CIB anisotropies (Planck intermediate results. XVII. 2014; Adak et al. 2024) and study its spectral energy distribution. Several other attempts have been made to obtain a clean map of CIB anisotropies by taking advantage of the full velocity coverage ($|v_{LSR}| < 600\mathrm{km s}^{-1}$) of 21 cm H I observations (Planck early results. XXIV. 2011; Lenz et al. 2019; McCarthy 2024), where v_{LSR} is the velocity of the H I gas measured in the local standard of rest frame. The dust-CIB separation using the template-fit approach, however, becomes challenging when the zero level of the sky background is unknown and there are significant variations in the dust emissivity at high Galactic latitudes. Planck 2013 results. VIII. (2014) used a constant dust emissivity in very

⋆ Corresponding authors: sinha.srijita@niser.ac.in; tghosh@niser.ac.in

low H I column density regions ($N_{\rm H\,I} < 2 \times 10^{20}\,{\rm cm}^{-2}$) to set the zero level of the *Planck* intensity map at 857 GHz. *Planck* 857 GHz was then used as a reference to set the zero level of all other *Planck* high frequency instrument (HFI) intensity maps. More recently, Adak et al. (2024) generalised this approach by fitting a pixel-dependent dust emissivity and a global offset using the Galactic H I template within a Bayesian inference framework. The dust and CIB can be separated at the power spectrum level, where the H I power spectrum is used as a tracer of the dust power spectrum and subtracted from the total map to estimate the CIB power spectrum (Mak et al. 2017; Viero et al. 2019). Another model-independent approach used the generalized needlet internal linear combination method, which employs spatial information of the CIB in terms of its angular power spectrum to disentangle dust emission from CIB anisotropies (Planck intermediate results. XLVIII. 2016).

Another approach to separate dust emission from CIB anisotropies is to rely on scattering transform (ST) statistics. ST statistics are a family of low-variance summary statistics inspired by neural networks that efficiently characterise non-Gaussian processes (Bruna & Mallat 2013; Andén & Mallat 2014). ST statistics are constructed from convolutions with a set of pass-band wavelets that separate a signal into its different oriented scales, and non-linear operations, such as modulus, that characterise the interaction, that is, the statistical dependence, between these different scales (Cheng & Ménard 2021). Since their introduction in astrophysics, these statistics have consistently approached or reached the best possible performance in characterising, classifying, and inferring parameters in various domains, such as the interstellar medium (Allys et al. 2019; Regaldo-Saint Blancard et al. 2020; Saydjari et al. 2021; Lei & Clark 2023; Richard et al. 2025), the large-scale structures of the Universe (Allys et al. 2020; Eickenberg et al. 2022; Valogiannis & Dvorkin 2022), weak lensing (Cheng et al. 2020; Cheng & Ménard 2021), and the epoch of reionisation (Greig et al. 2022; Hothi et al. 2024).

Additionally, STs offer the ability to construct an approximate generative model of a given process from an estimate of its ST statistics (Bruna & Mallat 2018). This has been demonstrated for various physical processes, with models sometimes constructed from a single image (Allys et al. 2020; Cheng et al. 2024). Initially developed for two-dimensional (2D) planar data, these models have since been expanded to include multi-frequency data (Blancard et al. 2023), spherical data (Mousset et al. 2024; Campeti et al. 2025), and even spectroscopic data (Hothi et al. 2026). Simulated data in CMB studies showed that an ST generative model constructed from a single dust-foreground patch can suffice for training a neural network to distinguish primordial *B* modes from dust emission, even within a challenging mono-frequency approach (Jeffrey et al. 2021).

Moreover, new ST-based component-separation algorithms have been developed. Introduced in Regaldo-Saint Blancard, Bruno et al. (2021); Delouis et al. (2022) to separate Galactic dust emission from instrumental noise in *Planck* data, these versatile algorithms relied on pixel-space optimisation under ST statistics constraints to generate dust maps compatible with the data once added to the noise. In these papers, the ability of these algorithms to leverage the different non-Gaussian properties of different signals was emphasised by the fact that the separations were performed at a single frequency. Additionally, these separations were performed without assuming a prior model of the component of interest (dust, in this case). Recently, Auclair et al. (2024) used an ST-based algorithm to separate dust emission from CIB anisotropies in *Herschel* Spectral and Photometric Imaging Receiver (SPIRE) observations. A major success of this paper is that this separation was achieved by relying on observational data alone, first learning an ST-based CIB model from a sky region where this signal was dominant, and then using this model to separate Galactic dust emission and CIB in the Spider region. More recently, Tsouros et al. (2026) used the ST-based component-separation to recover the polarised dust emission from the *Planck* data at 353 GHz.

The main goal of this paper is to build on previous work and separate the Galactic dust emission in *Planck* 353 GHz data from the CIB anisotropies and instrumental noise. To do this, we first construct an ST-based contamination model of CIB and instrumental noise over a set of square patches, each with a sky area of 222 deg^2, in regions of low H I column density. Secondly, we use this contamination model to perform an ST-based component-separation in regions of intermediate H I column densities. We use the particular scattering covariance (SC) statistics, a subclass of the ST statistics. We work with *Planck* 353 GHz data smoothed to an angular beam resolution of 16.2′ (full width at half maximum; FWHM) to match the angular beam resolution of the H I emission maps. At this angular beam resolution, the CIB anisotropies dominate instrumental noise. Before applying the component-separation algorithm to the real *Planck* data, we successfully test it on the simulated *Planck* maps with different signal-to-noise (S/N) ratios of the dust emission with respect to the contamination.

The paper is organised as follows. In Sect. 2, we describe the *Planck* data and the external datasets (`HI4PI` and dust-reddening map at 100 µm). Section 3 briefly describes the results of the template-fit approach to obtain the contamination map (or dust-subtracted *Planck* map) at 353 GHz over the low H I column density regions. In Sect. 4, we estimate the statistical properties of the contamination map from a limited set of square patches and its sample variance. In Sect. 5 we briefly present the set of ST statistics. The component-separation algorithm using the ST statistics is described in Sect. 6. In Sect. 7, we apply our algorithm to *Planck* simulations at 353 GHz. We present and discuss the results of the dust-CIB separation obtained from the *Planck* 353 GHz observations in Sect. 8, and finally, we summarise our findings in Sect. 9.

2. Datasets

2.1. Planck data

We used the publicly available *Planck*[1] spectral matching independent component analysis (`SMICA`) CMB-subtracted intensity map from the Public Release 3 at 353 GHz (Planck 2018 results. I. 2020). The 353 GHz map is provided in `HEALPix`[2] (Górski et al. 2005) format at $N_{\rm side} = 2048$ (pixel size ∼1.7′) with an angular beam resolution of 4.82′ FWHM (Planck 2018 results. III. 2020; Planck 2018 results. IV. 2020). We then smoothed the map at an angular beam resolution of 16.2′ (by convolving it with an additional Gaussian beam of $\sqrt{(16.2')^2 - (4.82')^2} = 15.47'$) and downgraded it to $N_{\rm side} = 512$ (pixel size 6.8′). We converted the map from $K_{\rm CMB}$ to kJy sr^{-1} units using the conversion factors given in Planck 2013 results. IX. (2014). We retained the CIB monopole that was added by hand to the *Planck* data at 353 GHz. From the `HEALPix` map, we extracted 2D tangential projection square patches (256 × 256 pixels) centred around

[1] http://pla.esac.esa.int/pla
[2] http://healpix.sf.net

`HEALPix` pixel of $N_{\rm side} = 4$ using the `reproject` Python package (Robitaille et al. 2020). The pixel size for each square patch was 3.5′, resulting in a total patch area of 222 deg^2.

We used the end-to-end full focal plane 10 (FFP10) noise simulations at 353 GHz (Planck 2018 results. III. 2020) to estimate the variance of the instrumental noise in the *Planck* 353 GHz data. Similar to the *Planck* data, we first smoothed the noise maps with an additional Gaussian beam smoothing of 15.47′, reprojected them to $N_{\rm side} = 512$, and then extracted the 2D patches from them.

2.2. External datasets

We used the `HI4PI` full-sky map with a spectral resolution of 1.49 kms^{-1}, which combines the data from the Effelsberg–Bonn H I Survey (EBHIS; Winkel, B. et al. 2016) and the Galactic All-Sky Survey (GASS; McClure-Griffiths et al. 2009; Kalberla et al. 2010). The map is provided on the `HEALPix` grid at $N_{\rm side} = 1024$ (pixel size 3.4′) and a common angular beam resolution of 16.2′ (FWHM). The root mean square brightness temperature uncertainty is 43 mK. Along the optically thin line of sight, the total H I column density ($N_{\rm H\,I}$; in units of 10^{18} cm^{-2}) can be obtained by integrating the brightness temperature (T_b) over the velocity channels using the relation (Dickey & Lockman 1990)

$$N_{\rm H\,I} = 1.82 \int T_b \, {\rm d}v_{LSR}. \tag{1}$$

Following Hayakawa & Fukui (2024), we integrated T_b over two velocity ranges of the H I clouds: one range with a low velocity (LV; $|v_{LSR}| < 30$ kms^{-1}), and the other with an intermediate velocity (IV; 30 kms^{-1} $< |v_{LSR}| <$ 100 kms^{-1}). We ignored the high-velocity H I emission (HV; $|v_{LSR}| > 90$ kms^{-1}) as no significant dust emission is associated with the HV template (Wakker & Boulanger 1986; Planck early results. XXIV. 2011; Lenz et al. 2016; Hayakawa & Fukui 2024). The column densities associated with the LV and IV components are defined as $N_{\rm LV}$ and $N_{\rm IV}$, respectively. Finally, we downgraded the $N_{\rm LV}$ and $N_{\rm IV}$ maps to the `HEALPix` grid of $N_{\rm side} = 512$ and extracted 2D square patches centred around `HEALPix` pixel of $N_{\rm side} = 4$. We treated the two column density maps as the tracers of the dust emission. We used the sum of the $N_{\rm IV}$ and $N_{\rm LV}$ as a measure of $N_{\rm H\,I}$.

The all-sky Galactic dust-reddening map produced by Schlegel, Finkbeiner, & Davis (1998, hereafter SFD) at 100 μm has imprints of extragalactic large-scale structure (LSS) or CIB (Chiang & Ménard 2019). The CIB map at 100 μm ($r_{\rm LSS}$) was reconstructed by cross-correlating the SFD map with the spectroscopic galaxies and quasars in SDSS. The corrected SFD (CSFD) was produced by subtracting the CIB contamination from the SFD map[3] (Chiang 2023). We worked with a publicly available CSFD map and a 100 μm CIB map at a `HEALPix` resolution of $N_{\rm side} = 512$ and smoothed the two maps to a common angular beam resolution of 16.2′ (FWHM). The CSFD map was used as a tracer for the dust emission to produce the *Planck* simulations.

3. Contamination map from the template-fit approach

In this section, we briefly discuss how we obtained the contamination map (or dust-subtracted *Planck* map) at 353 GHz. We used the Adak et al. (2024) formalism to fit the pixel-dependent dust emissivity and a global offset over low $N_{\rm H\,I}$ regions ($N_{\rm H\,I} < 4 \times 10^{20}$ cm^{-2}) using the template-fit approach. We used LV and IV H I templates as a tracer for the dust emission. Because the LV and IV maps are full-sky maps, we easily included the northern and southern Galactic hemispheres in the analysis, and we hence increased the total sky coverage.

We followed the iterative correlation method of Planck intermediate results. XVII. (2014) to construct a global mask, which is defined as follows. Over the initial mask with $N_{\rm H\,I} < 4 \times 10^{20}$ cm^{-2}, we computed the pixel-dependent dust emissivity between the CMB-subtracted *Planck* intensity map at 353 GHz and the two H I templates, and we then subtracted the best-fit model from the *Planck* 353 GHz data to produce a residual map. We fit a Gaussian to the residuals, calculated its standard deviation ($\sigma_{\rm G}$), and removed pixels with absolute values greater than $5\sigma_{\rm G}$. We repeated the same procedure until all pixels in the residual map fell within $5\sigma_{\rm G}$ region of the Gaussian fit to the residuals. We arrived at a converged Galactic mask after five iterations, covering a region of ~13 800 deg^2. The total sky fraction covered by the unmasked pixels is $f_{\rm sky} = 0.33$.

We modelled the input CMB-subtracted *Planck* intensity data (m) at 353 GHz as the sum of the dust emission (s), CIB anisotropies (c), and the instrumental noise (n),

$$m = s + c + n. \tag{2}$$

The global offset of the map (including the CIB monopole) term was included in the signal term s. Using Adak et al. (2024) formalism, we sampled the joint probability distribution of the pixel-dependent dust emissivity and the global offset given the two H I templates and the input data. We modelled s as

$$s = \epsilon_{\rm LV} N_{\rm LV} + \epsilon_{\rm IV} N_{\rm IV} + O, \tag{3}$$

where $\epsilon_{\rm LV}$ and $\epsilon_{\rm IV}$ correspond to the dust emissivity associated with the LV and IV column density maps, respectively, and O is the global offset. We assumed that the two dust emissivities varied over the sky, but had fixed values within a 1.8° × 1.8° pixel area, corresponding to a single pixel area of a `HEALPix` $N_{\rm side} = 32$ map. The contributions of CIB anisotropies and instrumental noise were propagated through the noise covariance matrix (Adak et al. 2024). The emissivity maps are shown in Fig. A.1. The mean and 1σ standard deviation values of $\epsilon_{\rm LV}$ and $\epsilon_{\rm IV}$ of 2644 $N_{\rm side} = 32$ pixels over the northern Galactic hemisphere are 46.5 ± 13.3 and 9.2 ± 41.2 kJy sr^{-1}(10^{20} cm^{-2})$^{-1}$, respectively. The mean values of $\epsilon_{\rm LV}$ and $\epsilon_{\rm IV}$ of 2257 $N_{\rm side} = 32$ pixels over the southern Galactic hemisphere are 40.5 ± 10.3 and -17.2 ± 32.7 kJy sr^{-1}(10^{20} cm^{-2})$^{-1}$, respectively. We report a global offset value of $O = 119.3 \pm 0.2$ kJy sr^{-1} over the Galactic mask used in our analysis. Our value is very close to the CIB monopole of 130 kJy sr^{-1} added to the *Planck* map at 353 GHz based on the Béthermin et al. (2010) CIB model. The small difference between our estimate of the global offset and the CIB monopole term added by the *Planck* collaboration of roughly 10.7 kJy sr^{-1} (or 37.5 μK$_{\rm CMB}$) might indicate warm ionized medium associated dust emission at high Galactic latitude (Gaensler et al. 2008), as included in the *Planck* analysis (Planck 2018 results. XII. 2020).

We refer to the dust map estimated from the template-fit approach within the Bayesian inference framework as $s_{\rm B}$. Next, we subtracted $s_{\rm B}$ from the input CMB-subtracted map to obtain the residual map, $r_{\rm B} = m - s_{\rm B}$, which includes the CIB anisotropies, instrumental noise, and possible residual dust emissions (not correlated with the two H I templates). The expected

[3] https://doi.org/10.5281/zenodo.8207175

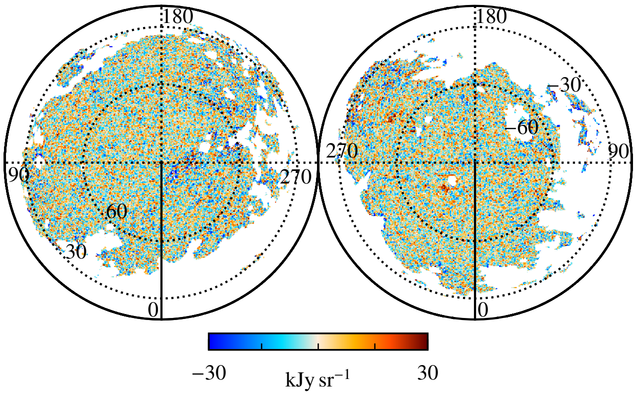

Fig. 1. Orthographic projection of the residual map obtained from the template-fit approach. The northern (southern) Galactic hemisphere is shown on the left (right). The white regions are masked from the analysis as they comprise $N_{\mathrm{H\,I}}$ cut-off pixels and the pixels were masked due to iterative masking.

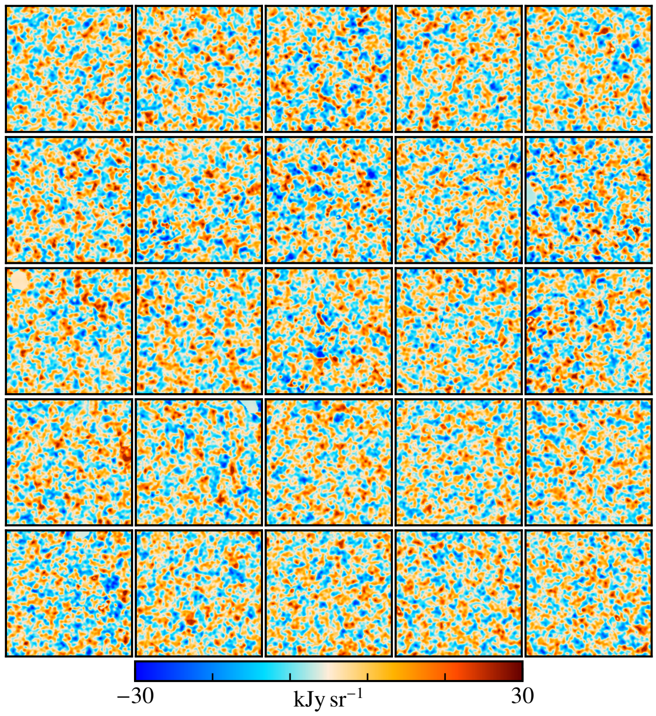

Fig. 2. Spatial distribution of the residual maps in the selected 25 square patches.

standard deviation of instrumental noise from FFP10 simulations over the Galactic mask is 3.3 kJy sr^{-1}, whereas the expected standard deviation of the CIB anisotropies based on the *Planck* 2013 best-fit CIB model (Planck 2013 results. XXX. 2014) is 9.3 kJy sr^{-1}. Because the standard deviation of two uncorrelated components is added in quadrature, we safely assumed that r_{B} map is dominated by the CIB anisotropies. The residual map at 353 GHz over the Galactic mask is shown in Fig. 1 in orthographic projection. With the two-template fit, we were able to extract the H I-correlated dust model map and the residual map over roughly twice the sky fraction as compared to the one-template fit analysis in the southern Galactic cap region (Adak et al. 2024). In both cases, the one-dimensional probability distribution of the residuals closely follows the Gaussian distribution. We computed the width of the Gaussian fit ($w_{r_{\mathrm{B}}}$) to the residuals over the common mask generated from the union of our iterative mask and southern Galactic cap region (Adak et al. 2024). We report a marginally smaller width in our analysis ($w_{r_{\mathrm{B}}}$ = 9.6 kJy sr^{-1}) as compared to the one-template fit analysis ($w_{r_{\mathrm{B}}}$ = 9.9 kJy sr^{-1}), indicating less leakage of Galactic emission in the residual map.

4. Statistical properties of the residual map over square patches

For our purpose, we first extracted 48 square patches (24 in the northern and 24 in the southern Galactic hemisphere) of size $14.9^{\circ} \times 14.9^{\circ}$ (sky area of 222 deg^2) centred around the centre of $N_{\mathrm{side}} = 4$ `HEALPix` grid pixels at high Galactic latitudes ($|b| > 45^{\circ}$). The pixel resolution of each square patch was $3.5'$ and contained 256×256 pixels. We note that $N_{\mathrm{side}} = 4$ pixels have a pixel size of $14.7^{\circ} \times 14.7^{\circ}$. All the square patches have very minimal overlap, and they hence provide an independent measurement of the statistical properties of the residual map at 353 GHz. We selected only 25 of these 48 square patches that were not severely affected by the initial mask to select the low $N_{\mathrm{H\,I}}$ regions and the pixels that were masked due to the iterative masking algorithm discussed in Sect. 3. Seventeen of these 25 square patches are completely unaffected by the final mask. Only a few pixels in the remaining 8 square patches are slightly affected by the final mask. The percentage of these masked pixels in these patches is lower than 1.5%. For these 25 square patches, the S/N defined as $\sigma_{s_{\mathrm{B}}}/\sigma_{r_{\mathrm{B}}}$ varies from 1 to 2.9.

As the template-fit approach was performed over an area of $1.8^{\circ} \times 1.8^{\circ}$ pixels, we expect some leakage of the Galactic dust emission from either the localised Galactic sources present in the *Planck* map below the 1.8° scale or the dust emission associated with molecular hydrogen (H_2) gas or ionised hydrogen (H II) into the residual map. To avoid Galactic residuals in the clean sky patches, we further applied a threshold mask to the 25 square patches. We excluded the pixels lying on the non-Gaussian tail part of the one-dimensional probability distribution function of r_{B} map by placing a threshold at $\pm 3\sigma_{r_{\mathrm{B}}}$. The percentage of the pixels that were masked due to the threshold mask ranges between 0.3% and 0.8%. We inpainted the masked pixels using linear interpolation with `griddata` function from `scipy.interpolate` package (Virtanen et al. 2020). Finally, the inpainted patches had no pixels that deviated by $\pm 3\sigma_{r_{\mathrm{B}}}$, which removed pixels containing contamination by the Galactic residuals. Figure 2 presents all the patches after inpainting was used to derive the statistical properties of the residual map. All the patches follow a Gaussian distribution with a mean standard deviation ($\sigma_{r_{\mathrm{B}}}$) of 8.9 kJy sr^{-1}. The estimated standard deviation of $\sigma_{r_{\mathrm{B}}}$ from these patches is 0.4 kJy sr^{-1}, which is much smaller than its mean value. We computed the power spectrum (C_{ℓ}) in these patches using the discrete Fourier transform in the flat-sky approximation (Hivon et al. 2002), implemented in the publicly available package `NaMaster`[4] (Alonso et al. 2019). As these patches do not obey periodic boundary conditions, we masked the boundary pixels in the computation of the power spectrum. We first made a binary mask considering only 180×180 inner pixels, as shown in the left panel of Fig. B.1. We then tapered the boundary with a cosine function to create the apodised mask (see the right panel of Fig. B.1). The errors on the power spectrum were computed from the analytic Gaussian covariance matrix

[4] https://github.com/LSSTDESC/NaMaster

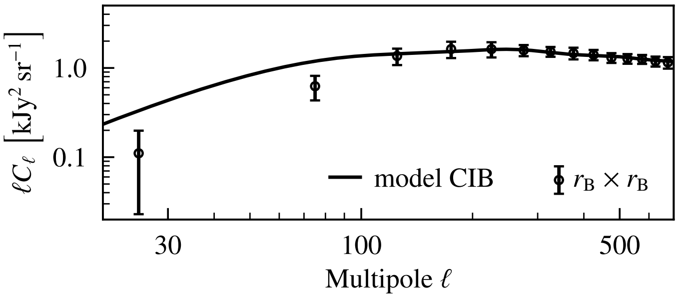

Fig. 3. Average power spectrum, in terms of ℓC_ℓ, with multipole ℓ over all the 25 selected square patches (black points). The error bars on them are the standard deviation obtained on the spectra. The solid black line represents the best-fit CIB model by Lenz et al. (2019) at 353 GHz.

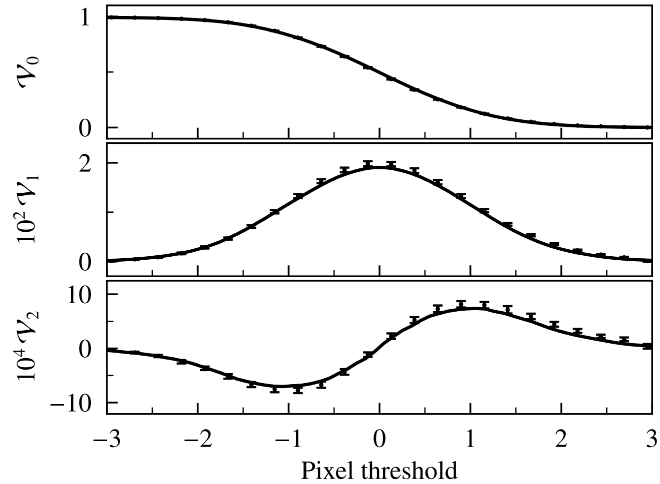

Fig. 4. Variation in $\mathcal{V}_0$, $\mathcal{V}_1$, and $\mathcal{V}_2$ with the pixel threshold of the MFs over all the 25 patches. The perimeter and Euler functions are scaled with 10^2 and 10^4, respectively, for visualisation purpose. The solid black line represents the MFs computed from the average of ten FFP10 noise-contaminated Gaussian CIB realisations over a given patch.

using `NaMaster`. We corrected the final power spectrum for the beam effect and the pixel window effect.

The average power spectrum of these patches is shown in Fig. 3. The sample variance of the power spectrum between all the patches agrees well for the spectra and is broadly consistent with the Lenz et al. (2019) best-fit CIB model (shown with a solid black line). At higher multipoles $\ell > 100$, our measurements of the average power spectrum of the residuals and the Lenz et al. (2019) CIB model match very well. We show the average power spectrum up to $\ell_{\max} = 700$ because the higher multipoles are significantly affected by the beam correction.

We computed the Minkowski functionals (MFs) for these patches. The MFs provide insight into the geometrical and topological structures of these regions as a variation in the pixel threshold value. For a 2D square patch, the MFs are the area ($\mathcal{V}_0$), perimeter ($\mathcal{V}_1$), and the Euler characteristic of the connected pixels and the number of holes in the same space or genus ($\mathcal{V}_2$). We used the publicly available package `QuantImPy` (Mantz et al. 2008; Boelens & Tchelepi 2021) to compute the MFs in these regions. Figure 4 shows the MFs of all the 25 selected square patches. We used the best-fit CIB model by Lenz et al. (2019) to generate ten Gaussian realisations of the CIB map and add ten non-Gaussian FFP10 noise realisations to it for a given patch. The solid black line in Fig. 4 shows the MFs obtained from the average of these ten noise-contaminated CIB realisations. As the instrumental noise is subdominant at the beam resolution we chose in our analysis, we conclude that the MFs of the 25 selected square patches closely follow the expected distribution from a Gaussian random field.

5. Scattering covariance statistics

We used the SC statistics introduced in Cheng et al. (2024) and Mousset et al. (2024). The SC statistics correspond to the covariances of terms constructed from a combination of convolutions of the input random field X with a set of pre-calculated wavelets and a non-linear modulus. The complex valued Morlet wavelet filters that we used, noted $\psi^{j,\gamma}$, are localised in pixel and harmonic space, and are characterised by a dyadic scale $j \in [0, J_{\max} - 1]$ and an orientation $\gamma \in [0, L-1]$. The wavelets probe characteristic scales of approximately 2^j pixels, and are oriented at an angle $\pi\gamma/L$ from the reference axis. $J_{\max} < \log_2(N)$ is the number of dyadic scales available for a given image of $N \times N$ pixels. There are four types of SC statistics. The first S_1 and S_2 statistics jointly characterise the amplitude and sparsity of the process X at a single oriented scale $\lambda = (j, \gamma)$. The higher-order wavelet moment estimators (S_3 and S_4) capture the interactions between two and three different oriented scales.

Auto and cross-ST statistics can be computed between two random fields X and Y. The cross SC statistics are defined as

$$\begin{aligned}
S_1^{\times,\lambda_1}(X,Y) &= \left\langle \left| \left(X * \psi^{\lambda_1}\right)\overline{\left(Y * \psi^{\lambda_1}\right)} \right| \right\rangle,\\
S_2^{\times,\lambda_1}(X,Y) &= \left\langle \left(X * \psi^{\lambda_1}\right)\overline{\left(Y * \psi^{\lambda_1}\right)} \right\rangle,\\
S_3^{\times,\lambda_1,\lambda_2}(X,Y) &= \mathrm{Cov}\left(X * \psi^{\lambda_1}, \left|Y * \psi^{\lambda_2}\right| * \psi^{\lambda_1}\right),\\
S_{3p}^{\times,\lambda_1,\lambda_2}(X,Y) &= \mathrm{Cov}\left(Y * \psi^{\lambda_1}, \left|X * \psi^{\lambda_2}\right| * \psi^{\lambda_1}\right),\\
S_4^{\times,\lambda_1,\lambda_2,\lambda_3}(X,Y) &= \mathrm{Cov}\left(\left|X * \psi^{\lambda_3}\right| * \psi^{\lambda_1}, \left|Y * \psi^{\lambda_2}\right| * \psi^{\lambda_1}\right),
\end{aligned} \tag{4}$$

where the asterisk stands for a convolution, the overbar is the complex conjugate, $\langle\cdot\rangle$ is the spatial average over the fields, and $\mathrm{Cov}(X, Y)$ is the estimated covariances of X and Y. For auto-SC statistics, S_1 and S_2 are simplified to

$$S_1^{\lambda_1}(X) = \left\langle \left|X * \psi^{\lambda_1}\right| \right\rangle, \quad \text{and} \quad S_2^{\lambda_1}(X) = \left\langle \left|X * \psi^{\lambda_1}\right|^2 \right\rangle, \tag{5}$$

while S_3 and S_4 were obtained by setting $X = Y$ in the previous equations, and the redundant S_{3p} terms was removed. Following previous work (Cheng et al. 2024; Mousset et al. 2024; Campeti et al. 2025), we normalised the $S_3^\times(X,Y)$ and $S_4^\times(X,Y)$ coefficients by their own $S_2^\times(X,Y)$ statistics,

$$\bar{S}_3^{\times,\lambda_1,\lambda_2} = \frac{S_3^{\times,\lambda_1,\lambda_2}}{\sqrt{S_2^{\times,\lambda_1} S_2^{\times,\lambda_2}}}, \quad \text{and} \quad \bar{S}_4^{\times,\lambda_1,\lambda_2,\lambda_3} = \frac{S_4^{\times,\lambda_1,\lambda_2,\lambda_3}}{\sqrt{S_2^{\times,\lambda_2} S_2^{\times,\lambda_3}}}. \tag{6}$$

As we worked with fields with 256×256 pixels, we set $J_{\max} = 5$ and $L = 4$ for the wavelet filters using the kernel size of 5×5 pixels. With these values of $J_{\max}$ and L, we obtained 2522 auto statistics and 2762 cross statistics. At the end, the final summary statistics Φ that we used for the cross statistics were the concatenation of the mean of the fields $\langle XY\rangle$, its variance $\mathrm{Var}(XY)$, and the normalised cross SC statistics, as

$$\Phi(XY) = \{\langle XY\rangle, \mathrm{Var}(XY), S_1^{\times,\lambda_1}, S_2^{\times,\lambda_1}, \bar{S}_3^{\times,\lambda_1,\lambda_2}, \bar{S}_{3p}^{\times,\lambda_1,\lambda_2}, \bar{S}_4^{\times,\lambda_1,\lambda_2,\lambda_3}\}. \tag{7}$$

For the auto statistics, the final summary statistics Φ were the concatenation of the mean of the field $\langle X\rangle$, its variance $\mathrm{Var}(X)$, and the normalised SC statistics, yielding

$$\Phi(X) = \{\langle X\rangle, \mathrm{Var}(X), S_1^{\lambda_1}, S_2^{\lambda_1}, \bar{S}_3^{\lambda_1,\lambda_2}, \bar{S}_4^{\lambda_1,\lambda_2,\lambda_3}\}. \tag{8}$$

We computed these summary statistics using the Python package `Foscat`[5] (Delouis et al. 2022; Campeti et al. 2025).

6. Component-separation algorithm

In this section, we present the component-separation algorithm based on SC statistics to statistically separate the dust emission from the contamination at 353 GHz *Planck* observations.

6.1. Generative contamination maps

We generated 300 synthetic contamination maps ($r_{\rm syn}$) from the 25 selected patches obtained in Sect. 4. These synthetic maps were constructed using maximum entropy generative models conditioned by the Φ statistics, as defined in Eq. (8) (we refer to Bruna & Mallat 2018; Cheng et al. 2024; Mousset et al. 2024 for more details).

We discuss below the steps that we followed to generate one of synthetic contamination maps. Starting from a white-noise realisation u_0, we performed a gradient descent in pixel space to minimise the following[6] loss function:

$$\mathcal{L}(u) = ||\Phi(r_{\rm B}) - \Phi(u)||^2, \tag{9}$$

where $||\cdot||$ is the Euclidean norm, and $r_{\rm B}$ is one of the residual patch. The samples of the generative models are the maps $r_{{\rm syn},i}$ obtained at the end of the optimisation, which verify

$$\Phi(r_{\rm B}) \approx \Phi\Big(r_{{\rm syn},i}\Big). \tag{10}$$

We optimised the loss function using the gradient descent algorithm in pixel space implemented in the `Foscat` package. The optimisation stopped when the difference of the loss functions in the two consecutive iterations was smaller than 10^{-6}.

6.2. Component-separation algorithm

We started with the data map m that we aimed to separate into the dust emission and the contamination. This was done by constructing maps that verified an ensemble of constraints that were constructed directly from the available data. The formalism for this statistical component-separation closely follows the formalisms presented in Delouis et al. (2022) and Auclair et al. (2024). We used six constraints to recover a dust map that was statistically compatible with the information available in the *Planck* data. The algorithm relies on a gradient descent on a running u map, which at the end of the optimisation corresponds to the recovered $\tilde{s}$ map of the dust emission. We write below the constraints that this $\tilde{s}$ map should fulfill, before expressing these constraints as losses involving the running u map. The first constraint ensures that the recovered signal added to the contamination statistically matches the data. In terms of the summary statistics, the constraint is written as

$$\Phi(m) \simeq \Big\langle \Phi\Big(\tilde{s} + r_{{\rm syn},i}\Big)\Big\rangle_{i\in N}, \tag{11}$$

where $\langle\cdot\rangle_i$ is the ensemble average over the N $r_{\rm syn}$ maps obtained in Sect. 6.1. The second constraint imposes that the cross-correlation between the data and the signal is conserved,

$$\Phi(m, \tilde{s}) \simeq \Big\langle \Phi\Big(\tilde{s} + r_{{\rm syn},i}, \tilde{s}\Big)\Big\rangle_{i\in N}. \tag{12}$$

The third constraint imposes that the statistics of the residual map $\tilde{r} = (m - \tilde{s})$ matches those of the $r_{\rm syn}$. This constraint ensures minimum leakage of the contamination into the recovered dust map. Mathematically,

$$\Phi(m - \tilde{s}) \simeq \Big\langle \Phi\Big(r_{{\rm syn},i}\Big)\Big\rangle_{i\in N}. \tag{13}$$

The fourth constraint enforces that the recovered dust map retains the same correlation with the total $N_{\rm H\,I}$ map as present in the data. The assumption here is that the contamination maps, being independent from the total $N_{\rm H\,I}$, can be sampled again without modifying the estimate of the cross statistics. Mathematically, it is written as

$$\Phi(N_{\rm H\,I}, m) \simeq \Big\langle \Phi\Big(N_{\rm H\,I}, \tilde{s} + r_{{\rm syn},i}\Big)\Big\rangle_{i\in N}. \tag{14}$$

The fifth constraint is that the residual map is uncorrelated with the $N_{\rm H\,I}$ map, which yields

$$\Phi(N_{\rm H\,I}, m - \tilde{s}) \simeq \Big\langle \Phi\Big(N_{\rm H\,I}, r_{{\rm syn},i}\Big)\Big\rangle_{i\in N}. \tag{15}$$

Finally, the sixth constraint imposes that the residual map is uncorrelated with the dust map separately,

$$\Phi(\tilde{s}, m - \tilde{s}) \simeq \Big\langle \Phi\Big(\tilde{s}, r_{{\rm syn},i}\Big)\Big\rangle_{i\in N}. \tag{16}$$

The last four constraints enforce minimum leakage of the dust signal into the contamination map at the angular scales at which the amplitude of the dust signal is comparable to that of the contamination.

Following Delouis et al. (2022), the mathematical loss functions corresponding to these constraints are respectively written as

$$\begin{aligned}
\mathcal{L}_1(u) &= \left\|\frac{\Phi(m) - \Phi(u) - B_1}{\sigma_{\Phi(u+r_{{\rm syn},i})}}\right\|^2, \\
B_1 &= \Big\langle \Phi(u + r_{{\rm syn},i}) - \Phi(u)\Big\rangle_{i\in N} \\
\mathcal{L}_2(u) &= \left\|\frac{\Phi(m,u) - \Phi(u,u) - B_2}{\sigma_{\Phi(u+r_{{\rm syn},i},u)}}\right\|^2, \\
B_2 &= \langle \Phi(u + r_{{\rm syn},i}, u) - \Phi(u,u)\rangle_{i\in N}, \\
\mathcal{L}_3(u) &= \left\|\frac{\Phi(m-u) - \Big\langle \Phi(r_{{\rm syn},i})\Big\rangle_{i\in N}}{\sigma_{\Phi(r_{{\rm syn},i})}}\right\|^2, \\
\mathcal{L}_4(u) &= \left\|\frac{\Phi(N_{\rm H\,I}, m) - \Phi(N_{\rm H\,I}, u) - B_4}{\sigma_{\Phi(N_{\rm H\,I}, u+r_{{\rm syn},i})}}\right\|^2, \\
B_4 &= \Big\langle \Phi(N_{\rm H\,I}, u + r_{{\rm syn},i}) - \Phi(N_{\rm H\,I}, u)\Big\rangle_{i\in N}, \\
\mathcal{L}_5(u) &= \left\|\frac{\Phi(N_{\rm H\,I}, m-u) - \langle \Phi(N_{\rm H\,I}, r_{{\rm syn},i})\rangle_{i\in N}}{\sigma_{\Phi(N_{\rm H\,I}, r_{{\rm syn},i})}}\right\|^2, \\
\mathcal{L}_6(u) &= \left\|\frac{\Phi(u, m-u) - \langle \Phi(u, r_{{\rm syn},i})\rangle_{i\in N}}{\sigma_{\Phi(u, r_{{\rm syn},i})}}\right\|^2.
\end{aligned} \tag{17}$$

[5] https://github.com/jmdelouis/FOSCAT

[6] In addition to the normalisation of the SC statistics described Eq. (6), we take here the log of the S_1 and S_2 coefficients.

We minimised the total loss function, given as

$$\mathcal{L}(u) = \mathcal{L}_1(u) + \mathcal{L}_2(u) + \mathcal{L}_3(u) + \mathcal{L}_4(u) + \mathcal{L}_5(u) + \mathcal{L}_6(u). \quad (18)$$

For the detailed concept behind the bias B and standard deviation σ, we refer to Delouis et al. (2022). For example, the loss $\mathcal{L}_1$ is computed as the normalised chi-square distribution between $\Phi(m)$ and $\left\langle \Phi(u + r_{\mathrm{syn},i}) \right\rangle_{i \in N}$. However, for computational efficiency, it relies on an bias B_1, which is estimated only after a certain number of iterations. This avoids the need to trace $\left\langle \Phi(u + r_{\mathrm{syn},i}) \right\rangle_{i \in N}$ throughout the optimisation. This bias is only necessary when the loss involves an ensemble average over the $r_{\mathrm{syn},i}$ maps.

The different initial condition maps for the gradient descent were made from the m map smoothed with a W' (FWHM) Gaussian beam, where W was chosen randomly from a uniform distribution $\mathcal{U}[100, 200]$. Starting from the initial map u_0, we minimised the total loss function using the gradient descent algorithm in `Foscat`. The final dust map $\tilde{s}$ corresponded to u at the end of the optimisation, and the residual map was obtained as $\tilde{r} = (m - \tilde{s})$. In practice, we updated the B_1, B_2 and B_4 biases and all variance terms every 150 iterations. We ran this optimisation until the difference between two consecutive losses in an epoch was $\Delta\mathcal{L} < 0.002$. The typical number of epochs required to reach the $\Delta\mathcal{L}$ varied from five to eight, depending on the data map. Numerically, we found that decreasing $\Delta\mathcal{L}$ beyond 0.002 did not improve the recovered dust map. The total computation time ranged from 15 to 20 minutes on a single-node GPU cluster (`NVIDIA A30`), depending on the number of iterations performed.

7. *Planck* simulations

We first validated the component-separation algorithm described in Sect. 6.2 on simulated *Planck* maps on a 2D square patch.

7.1. Synthetic contamination maps

We synthesised 12 statistically identical realisations from each sky patch considered in Sect. 3, totaling $N = 300$ realisations of r_{syn} maps using the summary statistics, as discussed in Sect. 6.1. The synthetic contamination maps retained the all the statistical properties of the r_{B} and had a mean standard deviation $\sigma_{r_{\mathrm{syn}}}$ of 9.0 kJy sr^{-1}, and the estimated 1σ variation in the $\sigma_{r_{\mathrm{syn}}}$ was 0.4 kJy sr^{-1}. These synthetic maps followed the Gaussian distribution and had the same one-dimensional probability distribution function as the r_{B} maps. We also computed the angular power spectra and the three MFs. They followed the mean r_{B} statistics. For brevity, we only show the mean and standard deviation of the S_1 and S_2 coefficients obtained from the 25 r_{B} and 300 r_{syn} maps in Fig. 5. We show the mean and standard deviation of the other two normalised coefficients $\bar{S}_3$ and $\bar{S}_4$ in Fig. C.1. We used these 300 r_{syn} maps to compute the variance on its summary statistics.

7.2. Simulated map at 353 GHz

We chose a test patch centred at Galactic coordinates $(l, b) = (45.0^\circ, -54.3^\circ)$ of sky area 222 deg^2. The mean H I column density over the entire patch was $\langle N_{\mathrm{H\,I}} \rangle = 3.3 \times 10^{20}$ cm^{-2}. We extracted the same sky patch from the CSFD map and scaled it with a constant factor to produce an input dust map. We kept the contamination map fixed and varied the dust amplitude to

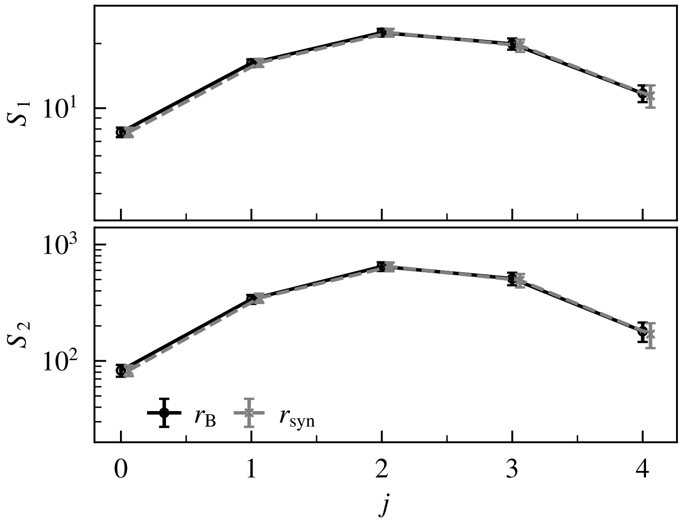

Fig. 5. Comparison of the S_1 and S_2 statistics of mean and standard deviation of 25 contamination maps obtained from the template-fit approach r_{B} regions (black circles) and 300 synthetic contamination maps r_{syn} (grey crosses). The grey crosses are shifted in the x-axis.

produce different S/N maps. The constant scaling factor controls the S/Ns of the input dust map with respect to the contamination.

We validated our algorithm for S/Ns 3 to 9. We discuss the S/N = 3 results in detail and highlight the primary differences among the others. We call the scaled 2D input dust map s_{sim}, to which we added a realisation of the contamination map (r_{sim}) from the generative model r_{syn} obtained in Sect. 7.1 to produce the contaminated map ($m_{\mathrm{sim}} = s_{\mathrm{sim}} + r_{\mathrm{sim}}$). The Pearson correlation coefficient ρ of s_{sim} with the $N_{\mathrm{H\,I}}$ map for S/N = 3 is 0.94 and was reduced to 0.88 after we added the contamination map r_{sim}. The top panel of Fig. 6 shows the input dust map at S/N = 3, one random realisation of the contamination, and the total contaminated simulated map. m_{sim} map is patchy owing to contamination.

7.3. Validating the component-separation algorithm

We applied the component-separation algorithm described in Sect. 6.2 to the contaminated map to extract a statistical realisation of the dust signal. By performing the component-separation under different initial conditions, we obtained 25 recovered dust maps. The bottom panel of Fig. 6 shows one of the recovered dust maps ($\tilde{s}_{\mathrm{sim}}$), the residual map ($\tilde{r}_{\mathrm{sim}} = m_{\mathrm{sim}} - \tilde{s}_{\mathrm{sim}}$), and the difference between the input and recovered dust ($\delta_s = \tilde{s}_{\mathrm{sim}} - s_{\mathrm{sim}}$). We clearly see some Galactic residuals near the boundaries of $\tilde{r}_{\mathrm{sim}}$ map. To avoid these boundary pixels, we restricted our analysis to the unmasked pixels within the binary mask (shown in the left panel of Fig. B.1) to compute the Pearson correlation coefficients. The value of ρ between s_{sim} and $\tilde{s}_{\mathrm{sim}}$ was found to be 0.97, showing a tight pixel-to-pixel correlation between the input and recovered dust maps. Visually, the small-scale features dominated by contamination are well separated from the large-scale dust emission. The δ_s map has no visible large-scale features at the map level. The correlation coefficient $\rho = 0.91$ between $\tilde{s}_{\mathrm{sim}}$ and $N_{\mathrm{H\,I}}$ is the same as was obtained between s_{sim} and $N_{\mathrm{H\,I}}$. This shows that the component-separation algorithm removes most of the contamination from the total map. The top panel of Fig. 7 shows the auto spectra ℓC_ℓ of r_{sim}, $\tilde{r}_{\mathrm{sim}}$, and δ_s, along with the magnitude of the cross-spectrum of r_{sim} with δ_s. The bottom panel presents the cross-spectra $\ell^2 C_\ell$ of δ_s and $\tilde{r}_{\mathrm{sim}}$ with the $N_{\mathrm{H\,I}}$

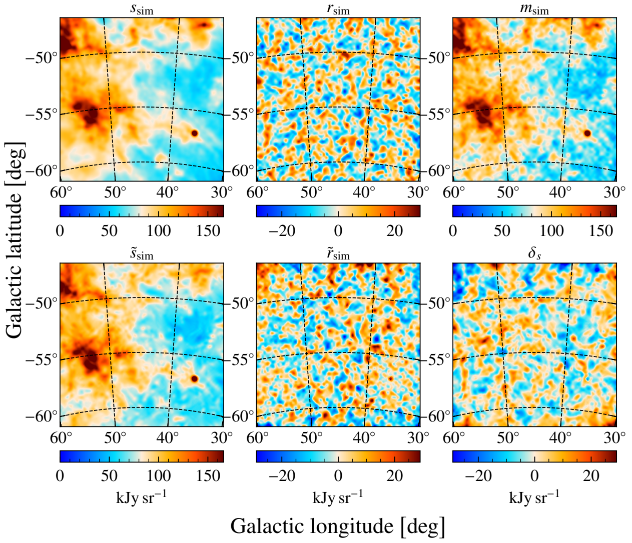

Fig. 6. *Top*: input maps at S/N = 3 centred around the sky patch at $(l, b) = (45.0°, -54.3°)$. The columns from *left to right* show the input dust map ($s_{\rm sim}$), the input contamination map ($r_{\rm sim}$), and the total simulated map ($m_{\rm sim}$). *Bottom*: columns from left to right: Component-separated dust map ($\tilde{s}_{\rm sim}$), residual map ($\tilde{r}_{\rm sim}$), and difference between input and recovered dust map (δ_s).

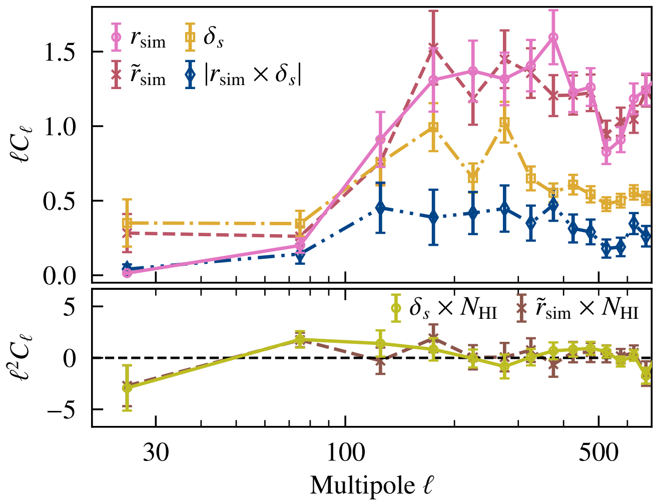

Fig. 7. *Top*: ℓC_ℓ spectra for $r_{\rm sim}$ (solid pink), $\tilde{r}_{\rm sim}$ (dashed red), δ_s (dashed-dotted orange), and magnitude of the cross-spectrum for $r_{\rm sim}$ and δ_s (dashed-dot-dotted blue) in kJy^2 sr^{-1}. *Bottom*: cross-spectra ($\ell^2 C_\ell$) of δ_s (solid green) and $\tilde{r}_{\rm sim}$ (dashed brown) with the $N_{\rm H\,I}$ map, in kJy sr$^{-1}\left(10^{20}\,{\rm cm}^{-2}\right)$.

map. We applied the apodised mask (Fig. B.1, right) to account for non-periodic boundaries. The power spectrum of the $r_{\rm sim}$ follows an $C_\ell \propto \ell^{-1.3}$ spectrum, which is consistent with the CIB model of Planck 2013 results. XXX. (2014). As our component-separation algorithm is a statistical method, the δ_s map captures the phase mismatch between the input and the output dust maps. The δ_s map is not correlated with $N_{\rm H\,I}$ map, as is captured by the cross-power spectrum of δ_s and $N_{\rm H\,I}$. The average δ_s map obtained from 25 realisations is shown in Fig. 8 (third column, top panel). The average δ_s map is also statistically uncorrelated with $N_{\rm H\,I}$ at the pixel level (bottom panel of Fig. 8). We show the comparison between the input and output dust spectra in Fig. C.2.

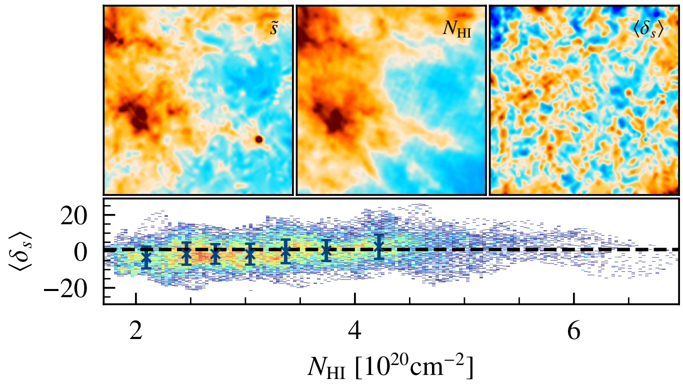

Fig. 8. *Top*: $\tilde{s}_{\rm sim}$ (left), H I column density map (middle), and the mean of 25 realisations of δ_s (right). *Bottom*: 2D correlation between $N_{\rm H\,I}$ and $\langle\delta_s\rangle$. The blue crosses and the error bars show the median values and standard deviations of mean $\langle\delta_s\rangle$ in the ordered bins of $N_{\rm H\,I}$.

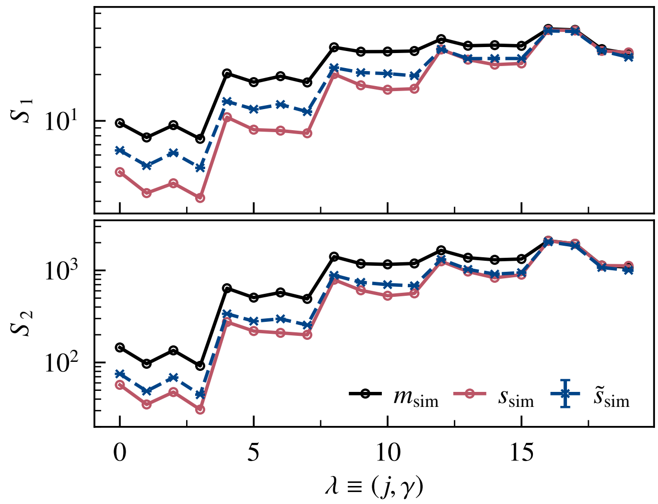

Fig. 9. Comparison of S_1 and S_2 statistics of $m_{\rm sim}$ (black circles), $s_{\rm sim}$ (red circles), and the $\tilde{s}_{\rm sim}$ (blue crosses with dashed line).

Next, we calculated the SC statistics (S_1, S_2, $\bar{S}_3$, and $\bar{S}_4$) of these maps. The mean and standard deviation of S_1 and S_2 for five different j values and four different γ values, computed from 25 recovered dust maps, are shown in Fig. 9. The x-axis represents $\lambda \equiv (j, \gamma)$, where $\lambda = 0$ corresponds to the smallest scale ($j = 0$) and the first wavelet orientation. Our component-separation algorithm accurately recovers these statistical properties of the dust map as a function of wavelet scales and orientations. The contamination in $m_{\rm sim}$ leads to higher S_1 and S_2 at small scales (or low j values) compared to $s_{\rm sim}$. The algorithm recovers almost all the scales of $s_{\rm sim}$, except for the smallest scales at S/N = 3. We show the remaining two SC statistics $\bar{S}_3$ and $\bar{S}_4$ in Fig. C.3. At S/N $\geqslant$ 5, the algorithm recovers S_1 and S_2 statistics for large and small scales. In Fig. C.4 we present the SC statistics for S/N = 5. The smallest scale ($j = 0$) between the input and output for all statistics agrees well. Figure 10 shows the angle-averaged S_1 and S_2 statistics of $r_{\rm sim}$ and $\tilde{r}_{\rm sim}$ for different values of j. As the contamination maps is statistically isotropic, there is no preferred orientation at which we expect to see more power. For $r_{\rm sim}$, we computed the 1σ standard deviation from 300 $r_{\rm syn}$ maps. In the same plot, we also show the same angle-averaged S_1 and S_2 cross statistics of the δ_s and $\tilde{r}_{\rm sim}$ maps. The cross S_1 and S_2 statistics between $r_{\rm sim}$ and $\tilde{r}_{\rm sim}$

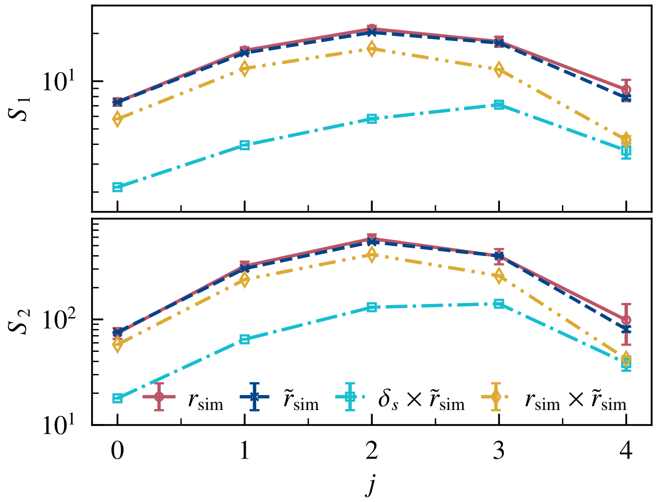

Fig. 10. Comparison of the angle-averaged S_1 and S_2 statistics of $r_{\rm sim}$ (red circles) and $\tilde{r}_{\rm sim}$ (blue crosses with the dashed line). The cyan squares with the dashed-dotted line show the cross coefficients between δ_s and $\tilde{r}_{\rm sim}$, and the orange diamonds with the dashed-dot-dotted line show that between $r_{\rm sim}$ and $\tilde{r}_{\rm sim}$.

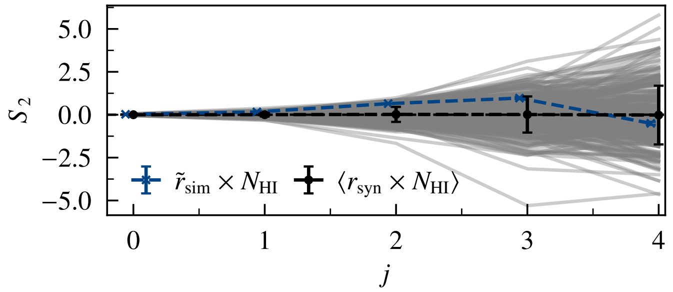

Fig. 11. Comparison of the angle-averaged S_2 cross statistics with the $N_{\rm H\,I}$ map: $\tilde{r}_{\rm sim}$ (dashed blue) and the mean over 300 $r_{\rm syn}$ (black). The recovered contamination is consistent with the expected statistics within 1σ. The blue crosses are slightly shifted along the x-axis. The grey lines show all 300 $r_{\rm syn}$ realisations.

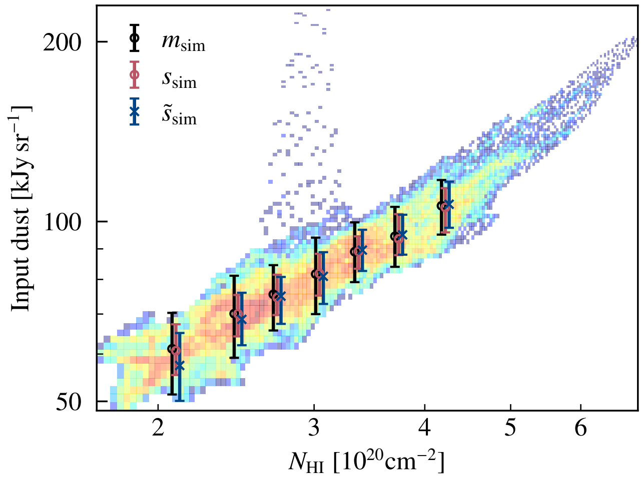

Fig. 12. 2D histogram showing the joint distribution of $s_{\rm sim}$ and $N_{\rm H\,I}$. The black circles correspond to the median values, and the upper and lower limits correspond to the 16 and 84 percentile of $m_{\rm sim}$ of the data in each ordered bin of $N_{\rm H\,I}$. Similarly, the red circles show $s_{\rm sim}$, and the blue crosses show $\tilde{s}_{\rm sim}$.

broadly follow the same statistics as $r_{\rm sim}$. This means that the $\tilde{r}_{\rm sim}$ map retains the phase information of the input $r_{\rm sim}$ up to a certain percentage. Even though δ_s visually appears to be similar to $r_{\rm sim}$, the S_2 amplitude of $\delta_s \times \tilde{r}_{\rm sim}$ is much smaller than the corresponding amplitude of $r_{\rm sim} \times r_{\rm sim}$ (or $\tilde{r}_{\rm sim} \times \tilde{r}_{\rm sim}$) at small scales corresponding to low j values. The 1σ deviation on the auto and cross statistics with the recovered maps was computed from the 25 realisations of $\tilde{r}$. Figure 11 shows the angle-averaged cross statistics S_2 between $\tilde{r}_{\rm sim}$ and $N_{\rm H\,I}$ map. The error bar on S_2 was computed from 25 realisations of the $\tilde{r}_{\rm sim}$, starting from different initial conditions. For completeness, we computed the expected cross statistics S_2 between $r_{\rm syn}$ and $N_{\rm H\,I}$ map. The mean value of the S_2 statistics computed from 300 $r_{\rm syn}$ maps is consistent with zero, and the 1σ error bars capture patch-to-patch variations of the same statistics. Since we added a single realisation of the contamination to the input dust map, the error bar on the $\tilde{r}_{\rm sim} \times N_{\rm H\,I}$ cross statistics S_2 only includes the statistical noise from the component-separation algorithm.

In Fig. 12, we plot the 2D histogram highlighting the joint distribution of $s_{\rm sim}$ and $N_{\rm H\,I}$, considering only the pixels those falls within the binary mask. This shows that the $s_{\rm sim}$ has a significant amount of scatter with $N_{\rm H\,I}$ over the entire patch, and the correlation between them becomes non-linear above $N_{\rm H\,I} > 4 \times 10^{20}{\rm cm}^{-2}$. Next, we binned the data into seven bins in order of increasing values of $N_{\rm H\,I}$ and computed the median values of $m_{\rm sim}$, $s_{\rm sim}$, and $\tilde{s}_{\rm sim}$ over each bin. The upper and lower limit of the error bars at each bin correspond to the 16 and 84 percentile of the three quantities $m_{\rm sim}$, $s_{\rm sim}$, and $\tilde{s}_{\rm sim}$. This plot shows that the distributions are very similar for these different maps, although there appears to be a consistent reduction in the standard deviation of the distribution at fixed $N_{\rm H\,I}$ values from $m_{\rm sim}$ to $\tilde{s}_{\rm sim}$. This effect is more pronounced in low $N_{\rm H\,I}$ regions, in which the contamination is comparable to the dust signal. The reduction of the error bars from $m_{\rm sim}$ to $\tilde{s}_{\rm sim}$ is consistent with the expected outcome of removing contaminants.

Next, we varied the S/N of the dust signal with respect to contamination. For each S/N, we quantified the reliability of the component-separation algorithm. For S/N $\geqslant 3$, we demonstrate that our component-separation algorithm successfully and efficiently separates the dust signal from the contamination at the level of summary statistics. The algorithm only recovers the dust signal at large scales for low S/Ns (S/N $\simeq 1$), leaving excess power at small scales in the recovered dust map. We applied the same procedure to other sky regions for different S/Ns and reached the same conclusions.

8. Application to *Planck* data

8.1. Component-separated maps and its summary statistics

In this section, we primarily focus on the component-separation results on a sky patch of 222 deg^2 area centred at Galactic coordinates $(l, b) = (247.5°, 66.4°)$ for brevity. We first subtracted the global offset term of 119.3 kJy sr^{-1} as obtained from the template-fit approach (see Sect. 3) from the CMB-subtracted *Planck* data to focus on the statistical separation of the dust emission and CIB contamination using the SC-based statistics. We refer to this map as $m_{\rm d}$. The mean H I column density measured across the entire map is $\langle N_{\rm H\,I} \rangle = 2.3 \times 10^{20}$ cm^{-2}. The Pearson correlation coefficient ρ between the $m_{\rm d}$ and $N_{\rm H\,I}$ maps is 0.84.

We applied the component-separation algorithm to extract a statistical realisation of the dust signal. We followed the same

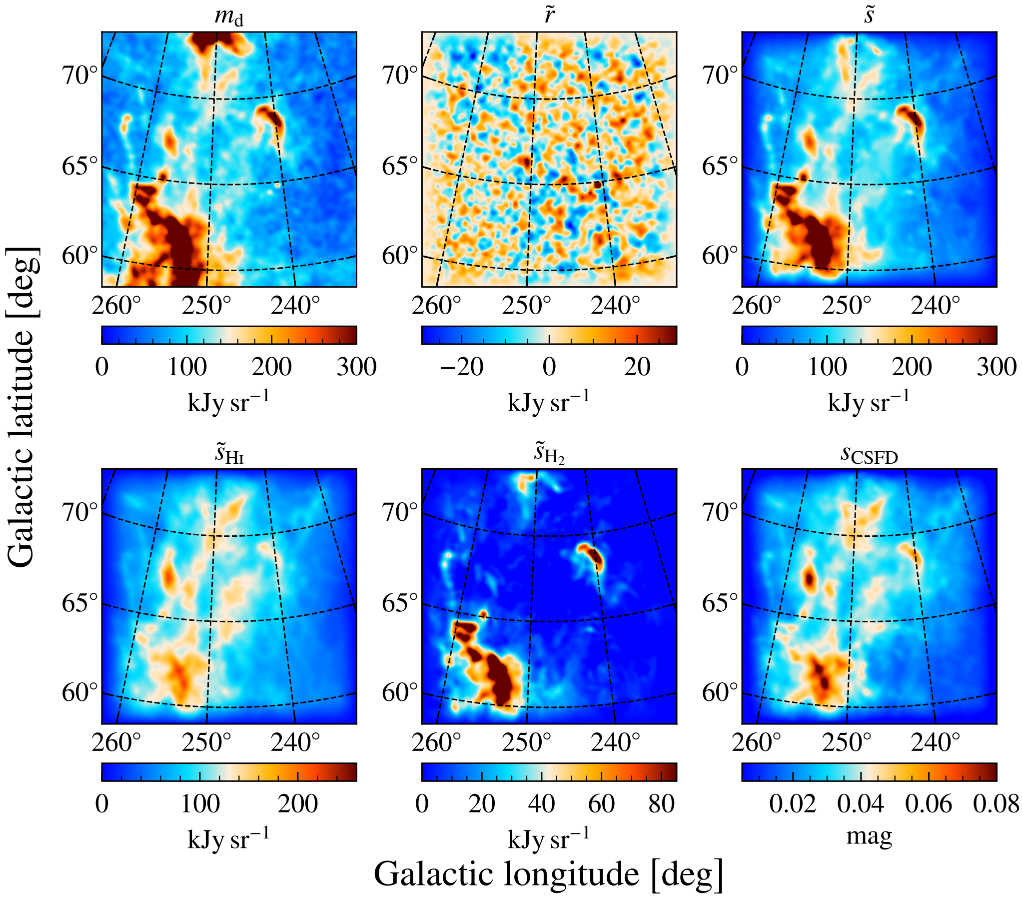

Fig. 13. *Top*: *Planck* 353 GHz map (CMB and global offset subtracted; left), $\tilde{r}$ (middle) and $\tilde{s}$ (right) after component-separation in the same sky region as in Fig. 6. *Bottom*: decomposed $\tilde{s}_{\rm H\,I}$ (left) and $\tilde{s}_{\rm H_2}$ maps (middle). The $s_{\rm CSFD}$ map at 100 µm (in mag units) in the same sky region is shown in the right panel.

steps as described in Sect. 7 and obtained 25 different realisations of dust map. The top panel of Fig. 13 shows the input map (m_d), recovered residual map ($\tilde{r}$) and a single realisation of the dust map ($\tilde{s}$). The recovered dust map retains most of the large-scale features present in the *Planck* data and filters out the small-scale fluctuations from the contamination. The mean dust emissivity over the entire sky patch was computed as the mean of the ratio of the recovered dust over $N_{\rm H\,I}$, defined as $\langle\epsilon\rangle = \langle\tilde{s}/N_{\rm H\,I}\rangle$. The mean value of the dust emissivity is $45\,{\rm kJy\,sr^{-1}}\left(10^{20}\,{\rm cm^{-2}}\right)$, which is consistent with the value obtained by Planck early results. XXIV. (2011); Planck intermediate results. XVII. (2014), and Adak et al. (2024).

Next, we present the statistics of the residual map ($\tilde{r}$). The top panel in Fig. 14 shows the joint distribution of $\tilde{r}$ and the $N_{\rm H\,I}$ map. The blue data points are the median values, and the error bars correspond to 1σ standard deviation in seven bins ordered in increasing values of $N_{\rm H\,I}$. The median values are consistent with zero, showing no significant leakage of $\tilde{s}$ into the residual map. The plot also confirms that our SC statistics-based component-separation algorithm works well for the S/N ≈ 8.4 region. The standard deviation of $\sigma_{\tilde{r}}$ over the masked region is $8.1\,{\rm kJy\,sr^{-1}}$, which is consistent with the expected value from 300 $r_{\rm syn}$ maps. In the middle panel of Fig. 14, we show the S_2 comparison of the $\tilde{r}$ map in the *Planck* field and the expected distribution from 300 $r_{\rm syn}$ maps. The amplitudes of the S_2 statistics match well at low j values, except at the very large scale ($j = 4$). The difference in S_2 statistics between the $\tilde{r}$ and 300 $r_{\rm syn}$ map is at the level of 2.3σ for $j = 4$. We also compared the $r_{\rm LSS}$ map at 100 µm from Chiang (2023) at that field. We multiplied the $r_{\rm LSS}$ map (in ${\rm kJy\,sr^{-1}}$ units) by a factor of 0.3 and computed the S_2 coefficient. We found that small-scale powers are missing from the $r_{\rm LSS}$ map, but the intermediate and large scales are consistent within the error bands from the synthetic maps. We correlated the $\tilde{s}$ map with $\tilde{r}$ map and found a cross-correlation coefficient $\rho = -0.06$ between the two maps. We show the cross S_2 statistics of $\tilde{s}$ and $\tilde{r}$ in the bottom panel of Fig. 14 to ensure that the recovered maps are statistically uncorrelated at the level of S_2 statistics. The 1σ deviations on the coefficients were computed from the cross S_2 statistics of $\tilde{s}$ and the 300 $r_{\rm syn}$ maps. We also computed the cross statistics S_2 between the $\tilde{s}$ and $r_{\rm LSS}$ map for the same sky patch. The 1σ deviations on S_2 were computed from the cross statistics of $\tilde{s}$ with 94 independent sky patches with a size of $14.9° \times 14.9°$ of the Chiang (2023) CIB/LSS map. All the scales are consistent with the zero within the 1σ error bar, except for the $j = 2$ scale, where the deviation is at the level of 3.2σ. The cross-correlation coefficient of the $\tilde{s}$ map with $r_{\rm LSS}$ map is $\rho = 0.03$.

We also performed a non-Gaussianity test to check for any significant leakage of the Galactic residuals into the $\tilde{r}$ map. The results of the non-Gaussianity test are presented in Appendix D. Additionally, we compared the statistics of the contamination maps from two different component-separation algorithms: the template-fit approach, and the SC-based statistics. In Appendix E, we present the component-separation results for the same *Planck* field as used to validate the component-separation algorithm in Sect. 7.

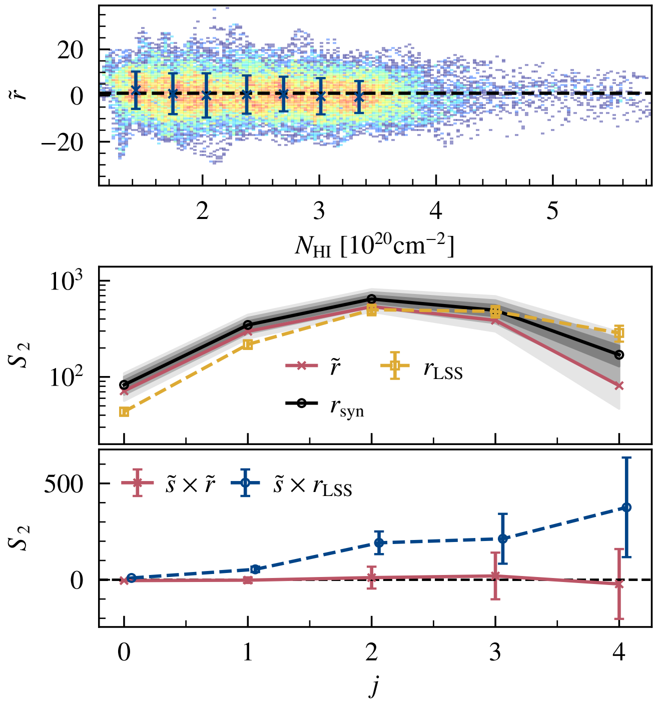

Fig. 14. *Top*: correlation plot of $\tilde{r}$ with $N_{\mathrm{H\,I}}$ map. The blue data points and the error bars show the zero median and standard deviation of $\tilde{r}$ in the ordered bins of $N_{\mathrm{H\,I}}$. The standard deviations are consistent in all the $N_{\mathrm{H\,I}}$ bins. *Middle*: comparison of angle-averaged S_2 statistics of $\tilde{r}$ (red cross), r_{LSS} (square dashed orange line) and the ensemble average of 300 r_{syn} maps (black circles) along with 1σ, 2σ, and 3σ error bands. *Bottom*: red crosses with the solid line show cross S_2 coefficients between $\tilde{s}$ and $\tilde{r}$, and the blue circles with the dashed line show the cross S_2 coefficients between $\tilde{s}$ and r_{LSS}. The blue circles are slightly shifted in the x-axis.

8.2. Separation in H I and H_2 emission

To understand the morphology of the recovered dust emission, we decomposed it into two components: dust associated with $N_{\mathrm{H\,I}}$ ($\tilde{s}_{\mathrm{H\,I}}$), and dust associated with $N_{\mathrm{H_2}}$ ($\tilde{s}_{\mathrm{H_2}}$),

$$\tilde{s} = \tilde{s}_{\mathrm{H\,I}} + \tilde{s}_{\mathrm{H_2}}, \tag{19}$$

where $\tilde{s}_{\mathrm{H\,I}} = \epsilon_{\mathrm{H\,I},353} N_{\mathrm{H\,I}}$, and $\epsilon_{\mathrm{H\,I},353}$ is the dust emissivity of the H I-correlated dust emission at 353 GHz. In our case, $\epsilon_{\mathrm{H\,I},353}$ is a constant value over the selected sky patch. We estimated the mean $\langle \epsilon_{N_{\mathrm{H\,I}},353} \rangle$ from the square patches, defined in Sect. 4, at high Galactic latitudes. We applied the final iterative mask (discussed in Sect. 3) to the high-latitude square patches to select only the low $N_{\mathrm{H\,I}}$ pixels where the dust–H I correlation holds. We also avoided square patches where more than 30% pixels were masked. Finally, we had 40 such high-latitude square patches with a sufficient number of valid pixels for the correlation analysis. Using a simple linear regression with the $N_{\mathrm{H\,I}}$ map, we found a value of the emissivity per square patch. While performing linear regression, we took the standard deviation of the contamination as an error bar per pixel into account. By analysing 40 sky patches, we obtained the mean and standard deviation of the dust emissivity as $\langle \epsilon_{\mathrm{H\,I},353} \rangle = 38 \pm 6\,\mathrm{kJy\,sr^{-1}} \left(10^{20}\,\mathrm{cm^{-2}}\right)$. We produced 25 realisations of the $\tilde{s}_{\mathrm{H\,I}}$ maps by varying $\epsilon_{\mathrm{H\,I},353}$ within the mean and standard deviation of this estimate. The bottom panel of Fig. 13 shows the decomposition of $\tilde{s}$ in terms of the $\tilde{s}_{\mathrm{H\,I}}$ (left panel) and $\tilde{s}_{\mathrm{H_2}}$ (middle panel) using the value of $\langle \epsilon_{\mathrm{H\,I},353} \rangle$. Visually, the $\tilde{s}_{\mathrm{H_2}}$ map is clumpy, whereas the $\tilde{s}_{\mathrm{H\,I}}$ map is more diffuse.

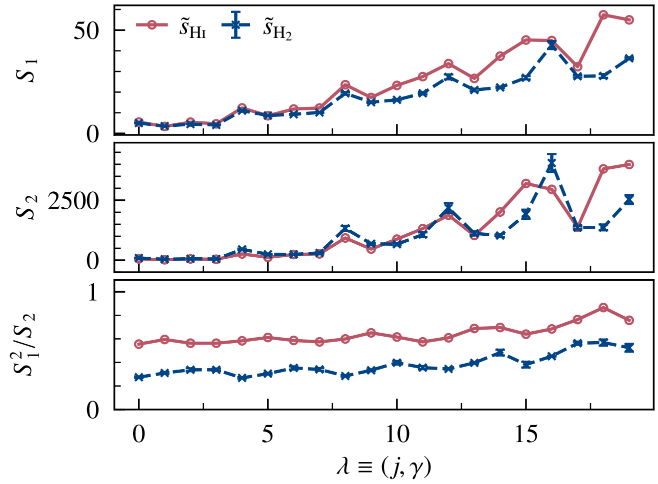

Fig. 15. S_1, S_2, and S_1^2/S_2 for the $\tilde{s}_{\mathrm{H\,I}}$ map (red circles) and the $\tilde{s}_{\mathrm{H_2}}$ maps (blue crosses with the dashed line). The standard deviation is obtained from 25 realisations of $\tilde{s}_{\mathrm{H_2}}$ maps.

We computed the SC statistics of the $\tilde{s}_{\mathrm{H\,I}}$ and $\tilde{s}_{\mathrm{H_2}}$ maps to characterise their morphological differences. We used the S_1 and S_2 statistics and the S_1^2/S_2 ratio to measure sparsity (Lei et al. 2025). Figure 15 shows the variation in S_1, S_2, and S_1^2/S_2 as a function of $\lambda \equiv (j, \gamma)$. The error bars on the SC statistics of the $\tilde{s}_{\mathrm{H_2}}$ map were computed from the 25 realisations of $\tilde{s}_{\mathrm{H_2}}$ maps. The first-order coefficient S_1 and wavelet power spectrum S_2 show that the $\tilde{s}_{\mathrm{H\,I}}$ map has more power at large angular scales and at all orientations than the $\tilde{s}_{\mathrm{H_2}}$ map. The lower values of the ratio S_1^2/S_2 for $\tilde{s}_{\mathrm{H_2}}$ compared to the $\tilde{s}_{\mathrm{H\,I}}$ map shows that $\tilde{s}_{\mathrm{H_2}}$ map is significantly sparser than $\tilde{s}_{\mathrm{H\,I}}$, as the ratio decreases with increasing sparsity of the field. This is consistent with Fig. 13, where the localised high column density structures are only present in the $\tilde{s}_{\mathrm{H_2}}$ map.

Next, we computed the power spectrum of $\tilde{s}$ and compared it with the power spectrum of $N_{\mathrm{H\,I}}$. Because of the limited sky coverage of the sky patch, the largest scale we obtained is $\ell \simeq 25$. We fitted them with a power-law model, $C_\ell \propto (\ell/75)^\alpha$, in the multipole range $25 \leqslant \ell \leqslant 625$ and found the best-fit value of the exponents as $\alpha_{\tilde{s}} = -2.51 \pm 0.07$ and $\alpha_{\mathrm{H\,I}} = -2.92 \pm 0.10$. The difference in the slope of $\tilde{s}$ and $N_{\mathrm{H\,I}}$ spectrum, $\Delta\alpha = \alpha_{\tilde{s}} - \alpha_{\mathrm{H\,I}} \approx 0.4$, also indicates a significant amount of dust emission associated with gas in the form of H_2 (Desert et al. 1988; Reach et al. 1998).

8.3. Comparison of our dust map with the CSFD extinction map

In this section, we compare the recovered *Planck* dust map at 353 GHz with the CSFD map at 100 µm over the same sky patch as discussed in Sect. 8.1. The right column of Fig. 13 shows the map-level comparison between $\tilde{s}$ (expressed in units of $\mathrm{kJy\,sr^{-1}}$) and s_{CSFD} (expressed in units of mag). Our first observation is that the *Planck* dust map contains more localised structures than the CSFD map. This finding is supported by the power spectrum comparison between the two maps. We computed the power spectrum of $\tilde{s}$ and s_{CSFD} over the apodised mask and fitted it with a power-law model within the multipole range $25 \leqslant \ell \leqslant 625$. The power spectrum exponent for the *Planck* dust map is $\alpha_{\tilde{s}} = -2.51 \pm 0.07$ and that for the CSFD map is $\alpha_{s_{\mathrm{CSFD}}} = -2.65 \pm 0.09$.

Next, we computed the non-linear dependence of $\tilde{s}$ and s_{CSFD} on the $N_{\mathrm{H\,I}}$ map by fitting a power-law model, $(\tilde{s}, s_{\mathrm{CSFD}}) \propto$

$\langle N_{\rm H\,I}\rangle^p$. The power-law exponent p is expected to be close to 1 in case of a tight correlation between dust and atomic gas. For each of the two dust maps, we grouped the pixel values into seven bins in ascending order of $N_{\rm H\,I}$ and computed the median values within each $N_{\rm H\,I}$ bin, as well as the 16 and 84 percentiles, which we used as error bars. We fitted the median values $\tilde{s}$ and $s_{\rm CSFD}$ with the mean $N_{\rm H\,I}$ (taking the error bars into account) and found that the value of the exponent p is 1.04 for the *Planck* map and 0.85 for the CSFD map. This result shows that the slope of the power law differs significantly between the *Planck* and CSFD maps. Furthermore, the data scatter in the $N_{\rm H\,I}$ correlation is greater for $\tilde{s}$ than for the $s_{\rm CSFD}$ map.

The morphological differences between the recovered *Planck* dust map and CSFD map can be explained by the different spectral energy distribution (SED) of H I-correlated dust emission and H_2-correlated dust emission. When the two SEDs follow the modified black-body spectrum (MBB), then the ratio of the emissivities of the H I and H_2-correlated dust components at 353 GHz can be written as

$$\frac{\epsilon_{\rm H\,I,353}}{\epsilon_{\rm H_2,353}} = \left(\frac{353}{\nu_0}\right)^{(\beta_{\rm H\,I}-\beta_{\rm H_2})} \frac{B_{353}(T_{\rm H\,I})}{B_{\nu_0}(T_{\rm H\,I})} \frac{B_{\nu_0}(T_{\rm H_2})}{B_{353}(T_{\rm H_2})}, \tag{20}$$

where $\nu_0 = 100\,\mu$m is the reference frequency, and $B_{353}(T)$ is the Planck black-body function at 353 GHz. Here, $(T_{\rm H\,I},\beta_{\rm H\,I})$ and $(T_{\rm H_2},\beta_{\rm H_2})$ are the temperatures and spectral indices of the H I and H_2-associated dust emission, respectively. We assumed that the ratio $\epsilon_{\rm H\,I,100\,\mu m}/\epsilon_{\rm H_2,100\,\mu m} = 1$. When we neglected the attenuation of the interstellar radiation field by dust within the diffuse interstellar medium, the integral of the MBB spectrum or the dust radiance (given by Eq. (10) in Planck 2013 results. XI. 2014) did not vary from H I to the H_2 gas. Under these two assumptions, the constraint relation between the SED parameters of H I and H_2-associated dust emission is

$$\frac{T_{\rm H_2}^{(\beta_{\rm H_2}+4)}\nu_0^{-\beta_{\rm H_2}}\Gamma(\beta_{\rm H_2}+4)\zeta(\beta_{\rm H_2}+4)}{T_{\rm H\,I}^{(\beta_{\rm H\,I}+4)}\nu_0^{-\beta_{\rm H\,I}}\Gamma(\beta_{\rm H\,I}+4)\zeta(\beta_{\rm H\,I}+4)} = 1. \tag{21}$$

We adopted $T_{\rm H\,I} = 20$ K and $\beta_{\rm H\,I} = 1.65$ from Planck intermediate results. XVII. (2014), computed from the MBB fit to the dust emissivities at the far-infrared frequencies 353, 545, and 857 GHz and COBE-DIRBE 100 µm for the H I-correlated dust emission. The change in $\beta_{\rm H_2}$ follows from that of $T_{\rm H_2}$, and thus, the change in relative grain emissivity at 353 GHz. We fitted the $s_{\rm CSFD}$ map with two templates ($\tilde{s}_{\rm H\,I}$ and $\tilde{s}_{\rm H_2}$) and a constant offset (O) over the valid pixels within the binary mask. We modelled the $s_{\rm CSFD}$ map as

$$\begin{aligned} s_{\rm CSFD} &= a_{\rm H\,I}\tilde{s}_{\rm H\,I} + a_{\rm H_2}\tilde{s}_{\rm H_2} + O, \\ &= a_{\rm H\,I}\epsilon_{\rm H\,I,353}\left(N_{\rm H\,I} + \frac{a_{\rm H_2}\tilde{s}_{\rm H_2}}{a_{\rm H\,I}\epsilon_{\rm H\,I,353}}\right) + O, \\ &= \epsilon_{\rm H\,I,100\,\mu m}(N_{\rm H\,I} + 2N_{\rm H_2}) + O. \end{aligned} \tag{22}$$

The best-fit values of $a_{\rm H\,I}$ is $0.32 \pm 0.06\,{\rm mag(MJy\,sr^{-1})^{-1}}$ and $a_{\rm H_2}$ is $0.0321 \pm 0.0003\,{\rm mag(MJy\,sr^{-1})^{-1}}$. By defining the diffuse H_2 column density map ($N_{\rm H_2}$) as $a_{\rm H_2}\tilde{s}_{\rm H_2}/(2a_{\rm H\,I}\epsilon_{\rm H\,I,353})$, we enforced the emissivities of H I and H_2-correlated dust emission to be the same at 100 µm. With $\tilde{s}_{\rm H_2} = \epsilon_{\rm H_2,353}(2N_{\rm H_2})$, the ratio of the H I-correlated dust emission and the H_2-correlated dust emission at 353 GHz is obtained as $\epsilon_{\rm H\,I,353}/\epsilon_{\rm H_2,353} = 0.11 \pm 0.01$. The observed ratio can be achieved by assuming that the H_2-correlated dust emission has a temperature of $T_{\rm H_2} = 18.5$ K and that the spectral index is $\beta_{\rm H_2} = 0.81$, which is different from the SED parameters of the H I-correlated emission. Recently, Sullivan et al. (2026) reported compelling evidence of two distinct dust emission components, which are referred to as hot and cold dust in the *Planck* data, lending further support to our results.

9. Summary and discussion

We statistically separated the dust signal from the CIB contamination at 353 GHz using the SC statistics. We used the $N_{\rm H\,I}$ map as an external tracer to minimise the leakage of the contamination into the recovered dust signal map. To do this, the component-separation algorithm relied on a set of loss functions so that the recovered dust map retained the spatial correlation, with the $N_{\rm H\,I}$ map as present in the input data, and the contamination was statistically uncorrelated with the $N_{\rm H\,I}$ map. A brief summary and the main results of the analysis are given below.

- We first analysed 25 square patches of the contamination map obtained at low $N_{\rm H\,I}$ regions using the template-fit approach, taking the pixel-dependent dust emissivity and a global offset into account. The standard deviation of the contamination map and its angular power spectrum obtained from 25 square patches are statistically consistent with each other. The three scalar MFs derived from these patches closely follow the expected values from a Gaussian distribution of CIB following the Lenz et al. (2019) best-fit CIB model plus instrumental noise contribution from FFP10 simulations;
- We synthesised 300 realisations of the contamination map using the scattering transform statistics based on the maximum entropy generative model. By construction, the 300 synthesised contamination maps followed the same summary statistics as the 25 contamination maps obtained from the template-fit approach at low $N_{\rm H\,I}$ regions;
- We validated our algorithm on a simulated 2D test patch centred at Galactic coordinates $(l, b) = (45.0^\circ, -54.3^\circ)$. We used the interstellar dust-reddening map from Chiang (2023) as a proxy of the dust emission and scaled its amplitude to different S/Ns with respect to the contamination map. We added a synthesised realisation of the contamination to the simulated dust map. We computed the SC statistics of the input and recovered dust maps and the cross SC statistics of the residual map with $N_{\rm H\,I}$ to conclude that the component-separation algorithm works fairly well for S/N $\geqslant 3$ case. There is no significant leakage of the dust emission into the contamination map. We verified that the recovered contamination map was uncorrelated with the $N_{\rm H\,I}$ map in the pixel space and in terms of S_2 statistics. We tested our component-separation algorithm on other sky patches and reached the same conclusions;
- We successfully applied the component-separation algorithm to a same test patch in the *Planck* data (S/N ≈ 8.4) and separated $\tilde{s}$ from $\tilde{r}$;
- We decomposed the component-separated *Planck* dust map at 353 GHz into a diffuse $\tilde{s}_{\rm H\,I}$ map and a clumpy $\tilde{s}_{\rm H_2}$ map. The significant amount of dust associated with H_2 gas in the $\tilde{s}$ can explain the difference in the power-law slopes of the $\tilde{s}$ and $N_{\rm H\,I}$ angular power spectra. We used the SC statistics to understand the morphological difference between the two components. The $\tilde{s}_{\rm H_2}$ map was found to be sparser but less filamentary in nature than the $\tilde{s}_{\rm H\,I}$ map;
- We also compared the component-separated dust map with the CSFD map at 100 µm for this region. The CSFD map is more tightly correlated with the $N_{\rm H\,I}$ map than the $\tilde{s}$ map. The

maps and the difference in power spectra exponents show that the $\tilde{s}$ has more localised structures in it than the CSFD map.

This paper opens the way to producing dust-reddening maps using the *Planck* data. The decomposition of the dust map (free from CIB contamination) into $N_{\mathrm{H\,I}}$ and $N_{\mathrm{H_2}}$ components helped us to investigate the formation of H_2 gas within the diffuse ISM. In a future paper, we will analyse all the available *Planck* high-frequency data ($\nu \geqslant 217$ GHz) to model the component-separated dust emission in terms of a modified black-body spectrum. The next step is to expand the dust-CIB separation problem to encompass the full sky using the software package `Foscat`. The production of clean dust maps, devoid of any CIB contamination, at all HFI frequencies is crucial for determining the spectral energy distribution of dust emission and for validating the dust-H I correlation in regions of low H I column density regions.

Acknowledgements. We thank Constant Auclair for the useful discussion and help during the start of the project. Some of the results in this paper have been derived using the `HEALPix` package. We acknowledge use of the *Planck* Legacy Archive. *Planck* is an ESA science mission with instruments and contributions directly funded by ESA Member States, NASA, and Canada. The Parkes Radio Telescope is part of the Australia Telescope National Facility which is funded by the Australian Government for operation as a National Facility managed by CSIRO. The EBHIS data are based on observations performed with the 100-m telescope of the MPIfR at Effelsberg. EBHIS was funded by the Deutsche Forschungsgemeinschaft (DFG) under the grants KE757/7-1 to 7-3. The computations in this paper were run on the GPU cluster at NISER supported by the Department of Atomic Energy of the Government of India. S.S. is supported by the National Postdoctoral Fellowship of the Science and Engineering Research Board (SERB), ANRF, Government of India (File No.: PDF/2023/000594). This work received government funding managed by the French National Research Agency under France 2030, reference numbers "ANR-23-IACL-0008" and "ANR-25-CE46-6634". The authors thank the anonymous referee for the helpful suggestions and constructive comments that improved the quality and clarity of this paper.

References

Adak, D., Shaikh, S., Sinha, S., et al. 2024, MNRAS, 531, 4876
Allys, E., Levrier, F., Zhang, S., et al. 2019, A&A, 629, A115
Allys, E., Marchand, T., Cardoso, J.-F., et al. 2020, Phys. Rev. D, 102, 103506
Alonso, D., Sanchez, J., Slosar, A., & Collaboration, L. D. E. S. 2019, MNRAS, 484, 4127
Andén, J., & Mallat, S. 2014, IEEE Trans. Signal Process., 62, 4114
Auclair, C., Allys, E., Boulanger, F., et al. 2024, A&A, 681, A1
Béthermin, M., Dole, H., Beelen, A., & Aussel, H. 2010, A&A, 512, A78
Blancard, B. R.-S., Allys, E., Auclair, C., et al. 2023, ApJ, 943, 9
Boelens, A. M. P., & Tchelepi, H. A. 2021, SoftwareX, 16, 100823
Boulanger, F., & Perault, M. 1988, ApJ, 330, 964
Boulanger, F., Abergel, A., Bernard, J. P., et al. 1996, A&A, 312, 256
Bruna, J., & Mallat, S. 2013, IEEE Trans. Pattern Anal. Mach. Intell., 35, 1872
Bruna, J., & Mallat, S. 2018, J. Math. Stat. Learn., 1, 257
Campeti, P., Delouis, J. M., Pagano, L., et al. 2025, A&A, 700, A136
Cheng, S., & Ménard, B. 2021, arXiv e-prints [arXiv:2112.01288]
Cheng, S., & Ménard, B. 2021, MNRAS, 507, 1012
Cheng, S., Ting, Y.-S., Ménard, B., & Bruna, J. 2020, MNRAS, 499, 5902
Cheng, S., Morel, R., Allys, E., Ménard, B., & Mallat, S. 2024, PNAS Nexus, 3, pgae103
Chiang, Y.-K., 2023, ApJ, 958, 118
Chiang, Y.-K., & Ménard, B. 2019, ApJ, 870, 120
Delouis, J.-M., Allys, E., Gauvrit, E., & Boulanger, F. 2022, A&A, 668, A122
Desert, F. X., Bazell, D., & Boulanger, F. 1988, ApJ, 334, 815
Dickey, J. M., & Lockman, F. J. 1990, ARA&A, 28, 215
Draine, B. T. 2011, Physics of the Interstellar and Intergalactic Medium
Eickenberg, M., Allys, E., Moradinezhad Dizgah, A., et al. 2022, arXiv e-prints [arXiv:2204.07646]
Gaensler, B. M., Madsen, G. J., Chatterjee, S., & Mao, S. A. 2008, PASA, 25, 184
Górski, K. M., Hivon, E., Banday, A. J., et al. 2005, ApJ, 622, 759
Greig, B., Ting, Y.-S., & Kaurov, A. A. 2022, MNRAS, 513, 1719
Hauser, M. G., & Dwek, E. 2001, Annu. Rev. Astron. Astrophys., 39, 249
Hayakawa, T., & Fukui, Y. 2024, MNRAS, 529, 1
Hivon, E., Górski, K. M., Netterfield, C. B., et al. 2002, ApJ, 567, 2
Hothi, I., Allys, E., Semelin, B., & Boulanger, F. 2024, A&A, 686, A212
Hothi, I., Allys, E., Semelin, B., & Meriot, R. 2026, A&A, 706, A15
Ichiki, K. 2014, Progr. Theor. Exp. Phys., 2014, 06B109
Jeffrey, N., Boulanger, F., Wandelt, B. D., et al. 2021, MNRAS, 510, L1
Kalberla, P. M. W., McClure-Griffiths, N. M., Pisano, D. J., et al. 2010, A&A, 521, A17
Lagache, G., Puget, J.-L., & Dole, H. 2005, Ann. Rev. Astron. Astrophys., 43, 727
Larsen, P., Challinor, A., Sherwin, B. D., & Mak, D. 2016, Phys. Rev. Lett., 117, 151102
Lei, M., & Clark, S. E. 2023, ApJ, 947, 74
Lei, M., Clark, S. E., Morel, R., et al. 2025, ApJ, 993, 4
Lenz, D., Doré, O., & Lagache, G. 2019, ApJ, 883, 75
Lenz, D., Flöer, L., & Kerp, J. 2016, A&A, 586, A121
Mak, D. S. Y., Challinor, A., Efstathiou, G., & Lagache, G. 2017, MNRAS, 466, 286
Maniyar, A. S., Béthermin, M., & Lagache, G. 2018, A&A, 614, A39
Mantz, H., Jacobs, K., & Mecke, K. 2008, J. Statist. Mech. Theory Exp., 2008, P12015
McCarthy, F. 2024, arXiv e-prints [arXiv:2405.13470]
McClure-Griffiths, N. M., Pisano, D. J., Calabretta, M. R., et al. 2009, ApJS, 181, 398
Mousset, L., Allys, E., Price, M. A., et al. 2024, A&A, 691, A269
Planck 2013 results. VIII. 2014, A&A, 571, A8
Planck 2013 results. IX. 2014, A&A, 571, A9
Planck 2013 results. XI. 2014, A&A, 571, A11
Planck 2013 results. XXX. 2014, A&A, 571, A30
Planck 2018 results. I. 2020, A&A, 641, A1
Planck 2018 results. III. 2020, A&A, 641, A3
Planck 2018 results. IV. 2020, A&A, 641, A4
Planck 2018 results. XII. 2020, A&A, 641, A12
Planck early results. XXIV. 2011, A&A, 536, A24
Planck intermediate results. XVII. 2014, A&A, 566, A55
Planck intermediate results. XLVIII. 2016, A&A, 596, A109
Puget, J. L., Abergel, A., Bernard, J. P., et al. 1996, A&A, 308, L5
Reach, W. T., Wall, W. F., & Odegard, N. 1998, ApJ, 507, 507
Regaldo-Saint Blancard, B., Levrier, F., Allys, E., Bellomi, E., & Boulanger, F. 2020, A&A, 642, A217
Regaldo-Saint Blancard, B., Allys, E., Boulanger, F., Levrier, F., & Jeffrey, N.. 2021, A&A, 649, L18
Richard, P., Allys, E., Levrier, F., Gusdorf, A., & Auclair, C. 2025, A&A, 696, A217
Robitaille, T., Deil, C., & Ginsburg, A. 2020, reproject: Python-based astronomical image reprojection, Astrophysics Source Code Library [record ascl:2011.023]
Saydjari, A. K., Portillo, S. K. N., Slepian, Z., et al. 2021, ApJ, 910, 122
Schlegel, D. J., Finkbeiner, D. P., & Davis, M. 1998, ApJ, 500, 525
Sullivan, R. M., Gjerløw, E., Galloway, M., et al. 2026, A&A, submitted [arXiv:2601.10640]
Tsouros, A., Russier, E., Allys, E., et al. 2026, arXiv e-prints [arXiv:2602.04528]
Valogiannis, G., & Dvorkin, C. 2022, Phys. Rev. D, 105, 103534
Viero, M. P., Reichardt, C. L., Benson, B. A., et al. 2019, ApJ, 881, 96
Virtanen, P., Gommers, R., Oliphant, T. E., et al. 2020, Nat. Methods, 17, 261
Wakker, B. P., & Boulanger, F. 1986, A&A, 170, 84
Winkel, B., Kerp, J., Flöer, L., et al. 2016, A&A, 585, A41

Appendix A: Emissivity maps

Figure A.1 shows the maps of LV-correlated and IV-correlated dust emissivity at `HEALPix` $N_{\rm side}$ = 32 pixel resolution. The white areas represent pixels excluded from the template-fit analysis after applying the iterative mask.

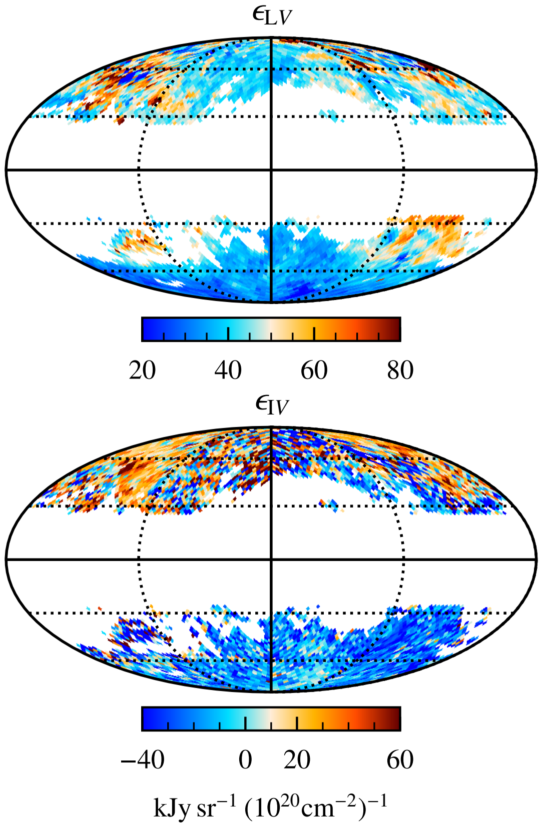

Fig. A.1. LV-correlated dust emissivity map ($\epsilon_{\rm LV}$; *top*) and IV-correlated dust emissivity map ($\epsilon_{\rm IV}$; *bottom*) obtained from the template-fit approach as discussed in Sect. 3. The $\epsilon_{\rm IV}$ map is mostly noisy in the southern Galactic hemisphere.

Appendix B: Masks

The binary and apodised masks used in this work are shown in Fig. B.1.

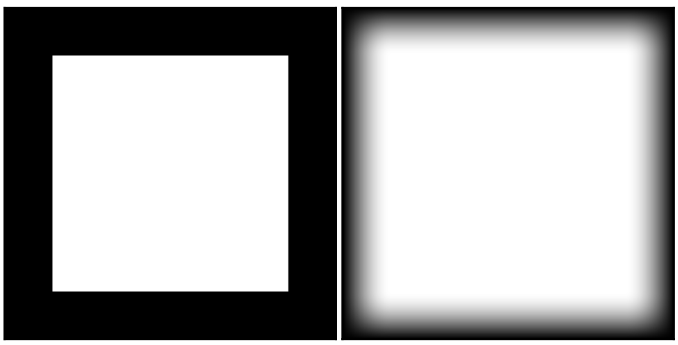

Fig. B.1. Binary mask (*left*) with inner 180 × 180 pixels and the 256 × 256 pixels apodised mask (*right*) used in our analysis.

Appendix C: Results for simulations

Appendix C.1: Synthetic contamination maps

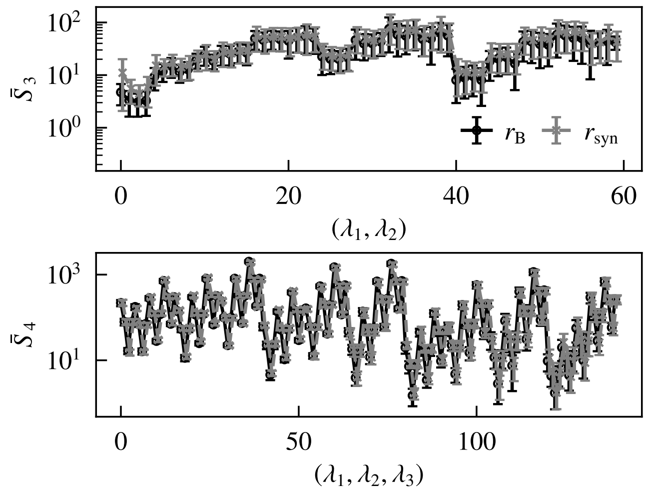

Fig. C.1. Same as Fig. 5 but for $\bar{S}_3$ and $\bar{S}_4$ statistics. The coefficients are obtained by averaging over angles. The grey crosses are shifted in the *x*-axis.

In Fig. C.1 we present the normalised SC statistics ($\bar{S}_3$ and $\bar{S}_4$) for 25 $r_{\rm B}$ regions and 300 $r_{\rm syn}$ maps, arranged in lexicographic order. As the contamination is independent of the wavelet orientations, the coefficients are averaged over angles. This demonstrates that the synthetic maps have identical SC statistics as the input contamination maps.

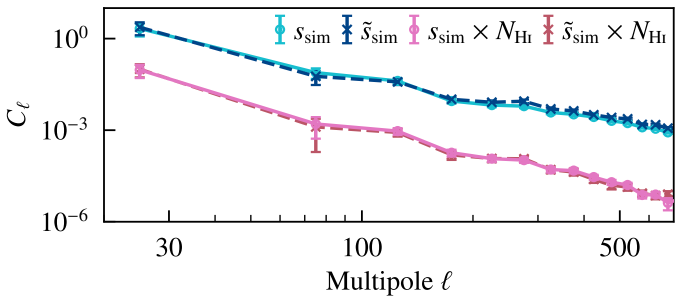

Fig. C.2. Angular power spectra C_ℓ vs. ℓ for input and output maps, showing auto-spectra of $s_{\rm sim}$ (cyan circles) and $\tilde{s}_{\rm sim}$ (blue crosses) and cross-spectra with the $N_{\rm H\,I}$ map (pink and red, respectively).

Appendix C.2: Validating the component-separation algorithm

Figure C.2 shows the power spectra of the input and output dust maps. The spectra for $s_{\rm sim}$ and $\tilde{s}_{\rm sim}$ are consistent. We also successfully recovered the input correlation with the $N_{\rm H\,I}$ map.

In Fig. C.3 we show the normalised SC statistics, $\bar{S}_3$ and $\bar{S}_4$, for $m_{\rm sim}$, $s_{\rm sim}$ and $\tilde{s}_{\rm sim}$ in lexicographic order. The algorithm preserves the correlations between the different wavelet scales present in $s_{\rm sim}$. Here, although the maps are anisotropic, we averaged over angles to reduce the number of coefficients and improve readability.

Figure C.4 shows the SC statistics (S_1, S_2, $\bar{S}_3$, and $\bar{S}_4$) for $m_{\rm sim}$, $s_{\rm sim}$ and $\tilde{s}_{\rm sim}$ at S/N = 5.

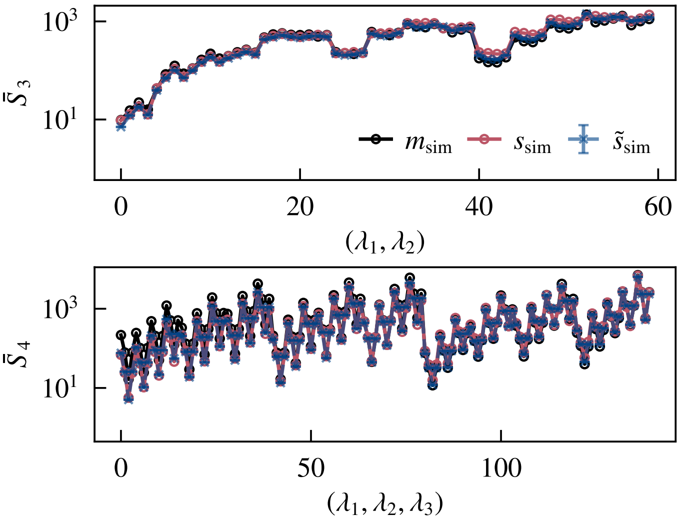

Fig. C.3. Comparison of $\bar{S}_3$ and $\bar{S}_4$ statistics between $m_{\rm sim}$, $s_{\rm sim}$ and $\tilde{s}_{\rm sim}$. To reduce the number of coefficients and improve readability, we average over angles.

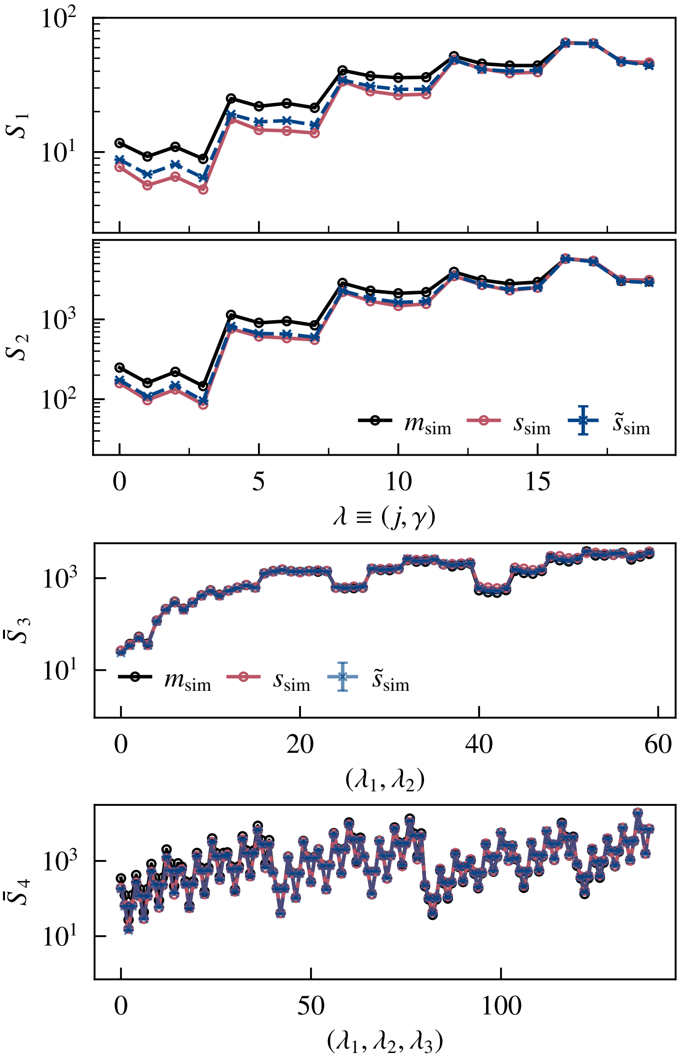

Fig. C.4. Summary statistics S_1, S_2, $\bar{S}_3$, and $\bar{S}_4$ for the S/N = 5 simulation case.

Appendix D: Statistics of the *Planck* contamination map

We compared the statistics of the recovered contamination map from SC-based component-separation method with the template-fit approach (discussed in Sect. 3) over the same *Planck* field as shown in Fig. 13. The histograms of the $r_{\rm B}$ and $\tilde{r}$ are shown in Fig. D.1 over the whole field and over the central unmasked region. From the histogram plot, it is clear that $r_{\rm B}$ is highly non-Gaussian (independent of the mask) due to the presence of the Galactic residuals (dark gas, molecular H_2 and ionised hydrogen). The distribution of $\tilde{r}$ map is close to the Gaussian once we exclude the boundary pixels. The black dotted line in Fig. D.1 is the Gaussian fit to the distribution of $\tilde{r}$ within the central unmasked region. Therefore, we can conclude that the SC-based component algorithm performs better than the template-fit approach in sky regions where excess H I-uncorrelated Galactic emissions are present. In Fig. D.2 we show the MFs of $\tilde{r}$

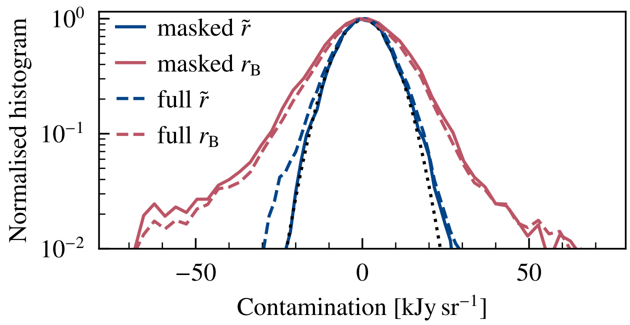

Fig. D.1. 1D distributions of $\tilde{r}$ (blue) and $r_{\rm B}$ (red). The solid lines show pixels within the binary mask and the dashed lines within the full region. The dotted black line is the Gaussian fit to the distribution of $\tilde{r}$ over the binary mask.

(dashed blue line), $r_{\rm B}$ (solid red line) and those from the 300 $r_{\rm syn}$ maps (solid grey lines) within the binary mask. The MFs of the $\tilde{r}$ map agree well with the 300 $r_{\rm syn}$ maps. Figures D.1 and D.2 demonstrate that the contamination map of the SC-based component-separation do not exhibit a non-Gaussian signature of Galactic emission.

Appendix E: Comparison of the component-separated *Planck* data results

For completeness, we showed the results of the component-separation algorithm for the *Planck* data region used to validate the component-separation algorithm in Sect. 7. Assuming the mean standard deviation of the contamination maps, $\sigma_{r_{\rm syn}}$ = 9.0 kJy sr^{-1}, this specific sky patch in the *Planck* data has an S/N ≈ 5. The first column of Fig. E.1 shows $m_{\rm d}$, second column shows $\tilde{s}$, and third column shows $\tilde{r}$, highlighting the difference between the *Planck* data and the recovered dust map. The first column of Fig. E.1 shows $m_{\rm d}$, second column shows $\tilde{s}$, and third column shows $\tilde{r}$, highlighting the difference between $m_{\rm d}$ and $\tilde{s}$. The standard deviation of $\tilde{r}$ computed over the binary mask is 8.3 kJy sr^{-1}, consistent with the expected standard deviation of the 300 $r_{\rm syn}$ that are used as an input to the component-separation algorithm.

The bright infrared point source centred at Galactic coordinates $(l, b) = (45.0°, -54.3°)$ is mostly present in the recovered dust map and a small fraction of it leaks into the residual map.

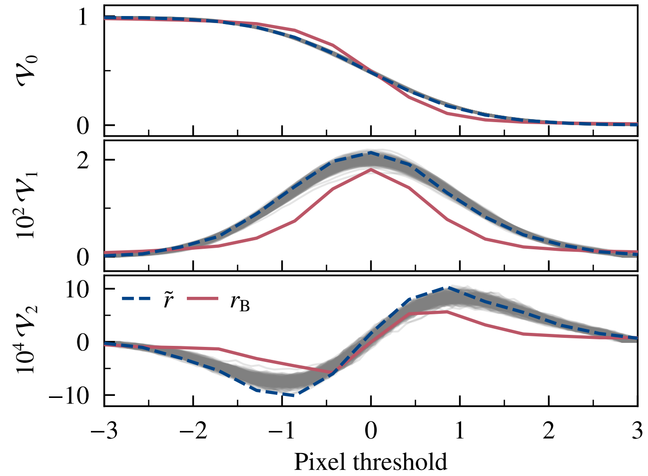

Fig. D.2. MFs of the $\tilde{r}$ (dashed blue line) and MFs of all 300 realisations of $r_{\rm syn}$ (grey lines). The three MFs of $\tilde{r}$ match well with the corresponding MFs of $r_{\rm syn}$ used as an input to the component-separation algorithm. The solid red line represents the MFs of the $r_{\rm B}$ map obtained from the template-fit approach.

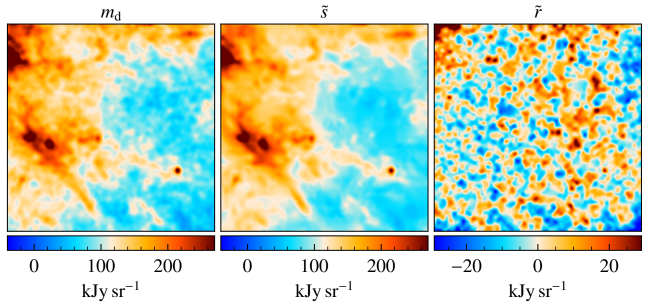

Fig. E.1. *Planck* data at 353 GHz (*left*), $\tilde{s}$ (*middle*), and $\tilde{r}$ (*right*) for the same sky region as used in Sect. 7.

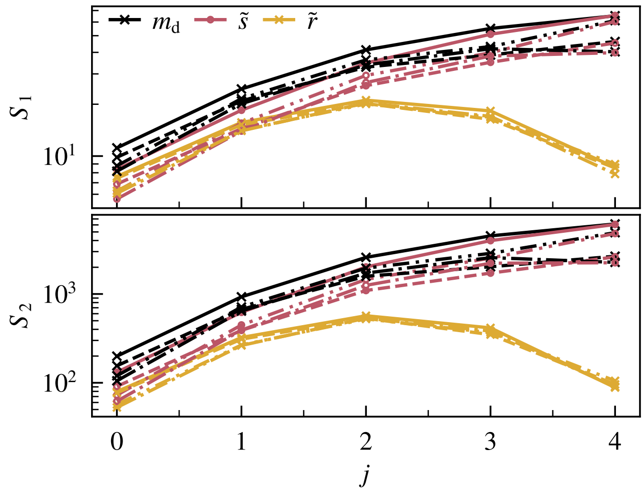

Fig. E.2. S_1 and S_2 coefficients of the $m_{\rm d}$, $\tilde{s}$, and $\tilde{r}$ maps. The four line types show the four different orientations.

We applied a 1° cut around the point source to exclude it from the further analysis of the summary statistics and the power spectrum. Figure E.2 shows the S_1 and S_2 coefficients for $m_{\rm d}$, $\tilde{s}$ and $\tilde{r}$ for the four different orientations of the wavelet. The $m_{\rm d}$ map at large scales (or high j values) is signal dominated. The contamination map, which is statistically isotropic, has roughly the same power in all four orientations.

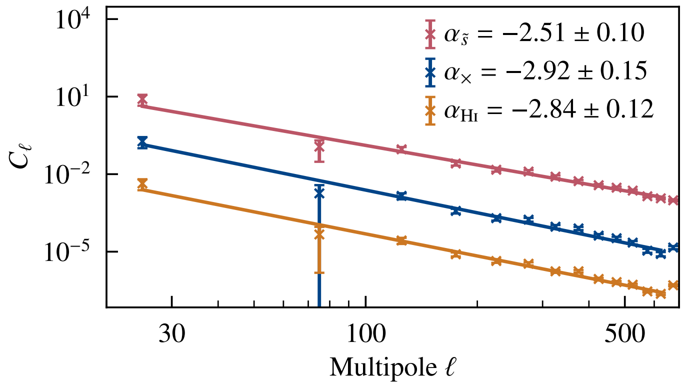

Fig. E.3. Auto spectrum C_ℓ with ℓ of $\tilde{s}$ (red crosses) and the best-fit power-law model (red line) in units of kJy^2 sr^{-1}. The blue shows the cross power spectrum of $\tilde{s}$ and the $N_{\rm H\,I}$ data along with the best-fit power-law model in kJy sr$^{-1}\left(10^{20}\,{\rm cm}^{-2}\right)$. The orange shows the auto spectrum of the total $N_{\rm H\,I}$ data with the best-fit model in $\left(10^{20}\,{\rm cm}^{-2}\right)^2$.

Figure E.3 shows the power spectra of $\tilde{s}$ and the $N_{\rm H\,I}$ data for the same region. We fitted the dust spectrum with the power-law model within the same multipole range as in Sect. 2.1. The straight lines in Fig. E.3 show the best-fit power-law models for the auto-power spectrum of $\tilde{s}$, cross-power spectrum of $\tilde{s}$ with $N_{\rm H\,I}$ map, and auto-power spectrum of the $N_{\rm H\,I}$ map. The best-fit exponents are $\alpha_{\tilde{s}} = -2.51 \pm 0.10$, $\alpha_\times = -2.92 \pm 0.15$ and $\alpha_{\rm H\,I} = -2.84 \pm 0.12$, respectively. In this case, the difference in the slopes of $\tilde{s}$ and $N_{\rm H\,I}$ spectra, $\Delta\alpha = \alpha_{\tilde{s}} - \alpha_{\rm H\,I} \approx 0.3$. We inferred that $\Delta\alpha \neq 0$ could be due to dust emission associated with H_2.